Department of Physics and Astronomy

Heidelberg University

Master thesis

in Physics

submitted by

Alexander Nies

born in Kirchen/Sieg

2021

Imaging of bromine oxide and formaldehyde using Fabry-Perot interferometer correlation spectroscopy

This Master thesis has been carried out by Alexander Nies

at the

Institute of Environmental Physics

under the supervision of

Prof. Dr Ulrich Platt

Imaging of bromine oxide and formaldehyde using Fabry-Perot interferometer correlation spectroscopy

Imaging of atmospheric trace gases in the UV and visible wavelength range provides insights into the spatial distribution of physical and chemical processes in the atmosphere. This is of particular advantage when observing fast-emitting point sources such as volcanoes. For this purpose, instruments are required that do not only combine a high spatio-temporal resolution with a high trace gas selectivity, but that are also robust and compact enough to be used in field measurements.
In this thesis, a prototype imaging instrument for formaldehyde (HCHO) and bromine oxide (BrO) based on Fabry-Perot interferometer correlation spectroscopy in the UV wavelength range is presented. The technique makes use of the periodic transmission spectrum of a Fabry-Perot-Interferometer and its correlation with the approximately periodic narrowband absorption structures of the target trace gas. This approach combines a high spatio-temporal resolution and a high spectral selectivity.
The feasibility of the technique is examined in a model study yielding instrument sensitivities of $k_{HCHO} = 1.82 \times 10^{-20} cm^2/molec$ and $k_{BrO} = 5.29 \times 10^{-18} cm^2/molec$ for HCHO and BrO, respectively. Furthermore, instrument characterization and testing in the laboratory shows good agreement between model and measurement.
Finally, first field studies with the prototype instrument reveals a detection limit for BrO of $1 \times 10^{14} molec/cm^2$ for a spatial resolution of 50×50 pixels and a temporal resolution of 10s. This should be sufficient to investigate BrO gradients in volcanic plumes with high halogen content and contribute to understanding the volcanic plume chemistry.

Bildgebung von Bromoxid und Formaldehyd mittels Fabry-Perot-Interferometer-Korrelationsspektroskopie

Zeitlich hoch aufgelöste, bildgebende Messungen von atmosphärischen Spurengasen liefert Einblicke in physikalische und chemische Prozesse in der Atmosphäre. Instrumente die für diesen Zweck entworfen sind, kombinieren idealerweise eine hohe räumliche und zeitliche Auflösung mit einer hohen Selektivität für das jeweilige Spurengas. Zusätzlich sollten die Instrumente kompakt und robust gebaut sein, um einen Betrieb im Feld zu gewährleisten.
In dieser Arbeit wird ein Prototyp eines bildgebenden Messinstrumentes für Formaldehyd (HCHO) und Bromoxid (BrO), basierend auf Fabry-Perot-Interferometer-Korrelations-Spektroskopie im UV Wellenlängenbereich, präsentiert. Diese Technik beruht auf dem periodischen Transmissionsspektrum eines Fabry-Perot-Interferometers und seiner Korrelation mit den nahezu periodischen schmalbandigen Absorptionsstrukturen des zu untersuchenden Spurengases. Durch diesen Ansatz wird hohe räumliche und zeitliche Auflösung mit hoher Selektivität erreicht. Die Anwendbarkeit der Messtechnik wird in einer Modellstudie untersucht. Diese liefert die folgenden Instrumentensensitivitäten $k_{HCHO} = 1.82 \times 10^{-20} cm^2/molec$ und $k_{BrO} = 5.29 \times 10^{-18} cm^2/molec$ für $HCHO$ und BrO. Zusätzlich ist der Instrumentenprototyp im Labor charakterisiert und getestet, wo eine gute Übereinstimmung zwischen Model und Messung gezeigt wird.
Zuletzt konnte aus ersten Feldmessungen eine Nachweisgrenze für BrO von $1 \times 10^{14} molec/cm^2$ für eine räumliche Auflösung von 50×50 Pixel und eine zeitliche Auflösung von 10s bestimmt werden. Dies sollte ausreichen um BrO Gradienten in Vulkanfahnen mit hohem Gehalt an Halogenen zu beobachten und damit einen Beitrag zum Verständnis der Chemie von Vulkanfahnen zu leisten.

Contents

1 Introduction

The main focus of this work is the development of an imaging instrument for bromine oxide (BrO) and formaldehyde (HCHO) based on Imaging Fabry-Perot-Interferometer Correlation Spectroscopy (IFPICS). The prototype presented in this work is the first imaging instrument of its kind. Building up such an instrument, laboratory and first field test measurements are the core of this master project.
Understanding of atmospheric processes remains a field with many open questions. Especially the role of trace gases has become a leading question of atmospheric physics, in particular their influence on atmospheric chemistry and radiative transfer in the context of climate change and air quality. Trace gases constitute about 0.1 % of the composition of our atmosphere. Besides rather long-lived trace gas species as carbon dioxide (CO_2) or methane (CH_4), many highly reactive species are present. Important species are halogen radicals, for example Br and Cl and their oxides BrO and ClO. Despite their short lifetime and low mixing ratios in the parts per trillion regime (ppt), their high reactivity has strong influences on the oxidizing capacity of the atmosphere. Several volcanoes are strong sources of halogen emissions that constitutes a complex study field due to the interaction of a special chemical composition with the ambient atmosphere. Due to the vast complexity of chemical reactions occurring inside a volcanic plume while volcanic gases mix with the ambient atmosphere the chemical evolution of volcanic plumes is still not well understood.
BrO can be measured relatively easily with remote sensing techniques (Differential Optical Absorption Spectroscopy, DOAS). These techniques allow for continuously monitoring of the BrO amount within a volcanic plume. However, its spatio-temporal resolution is too low to resolve chemical formation processes, which need to be understood in order to link the BrO amount in the volcanic plume to geophysical measures (e.g. the bromine emission). Fast and spatially resolved observation of BrO hence can yield important insights into the chemical processes in volcanic plumes. The ideal instrument for volcanic observations combines a high spatial resolution to cover the whole plume in one measurement, a high temporal resolution, to cover fast chemical processes and conversions and a high spectral selectivity because of the many trace gases abundant in volcanic plumes. In addition, the instrument must be light and mobile to be operated at remote locations under harsh environmental conditions. This thesis aims at building an instrument combining the above mentioned features.
The imaging Fabry-Perot interferometer correlation spectroscopy (IFPICS) technology combines the high spatio-temporal resolution of interference filter based SO_2 cameras (Bluth et al. (2007), Mori and Burton (2006)) with a high spectral se-

lectivity through the periodic transmission features of a Fabry-Perot interferometer (FPI). With this approach, the SO_2 camera technique should be expanded to weaker emitters and to other trace gases as for example to BrO or HCHO. The instrument prototype presented is based on work of Kuhn et al. (2014), Kuhn et al. (2019), Fuchs (2019) and Fuchs et al. (2021). Kuhn et al. (2014) and Kuhn et al. (2019) present the theoretical basis of the IFPICS technology for several trace gases and give a proof of concept for the detection of volcanic SO_2 with a one-pixel prototype instrument. Fuchs (2019) and Fuchs et al. (2021) build an imaging prototype instrument and shows the applicability of the IFPICS technique for imaging measurements of volcanic SO_2 emissions. This thesis presents a proof of concept of the IFPICS technology for other trace gases than SO_2 by imaging of HCHO gas cells and introduces first experiments of BrO imaging in volcanic plumes.
In chapter 1, the theoretical basis of this work is introduced by discussing the chemistry of volcanic plumes, radiative transfer in the atmosphere, common remote sensing techniques, imaging of trace gases and the IFPICS measurement principle. Chapter 2 explains the actual instrumental setup including a description of the individual parts and a complete characterization of the instrument. In chapter 3 the data evaluation process is explained in detail. In Chapter 4 and 5 the obtained measurements are presented: First, the proof of concept by imaging measurements of HCHO gas cells and second, with first field measurement results from experiments at Mt Etna, Italy.

1.1 Chemistry of volcanic plumes

Volcanoes emit large amounts of gases and aerosols this also includes various highly reactive trace gases. Sorted after the total amount, volcanoes emit vast quantities of CO_2, H_2O, SO_2, as well as a bunch of other trace gases including bromine, chlorine and iodine species (Oppenheimer et al., 2014). Volcanic plume chemistry ranges from high temperature reactions directly over vents or lava surfaces to multiphase reactions further downwind in the plume, caused by photochemistry, heterogenous reactions, and turbulent mixing with the ambient atmosphere. These emissions can have strong impacts on air quality and climate. Thus, this processes are very important for atmospheric chemistry.

Figure 1.1.1 illustrates an overview of bromine chemistry inside the volcanic plume, including mixing processes with the ambient atmosphere. As this thesis focusses on imaging measurements of BrO, the following part provides a short introduction to bromine chemistry based on Gutmann et al. (2018). BrO is not a primary emitted species, but the result of complex chemical processes within volcanic plumes. Halogens are mainly emitted as hydrogen halides, for example HBr. The formation of large amounts of BrO is explained with the autocatalytic reaction called *bromine explosion* known from polar and marine boundary layers Barrie et al. (1988). This cycle involves heterogenous reactions. A first reaction is the formation

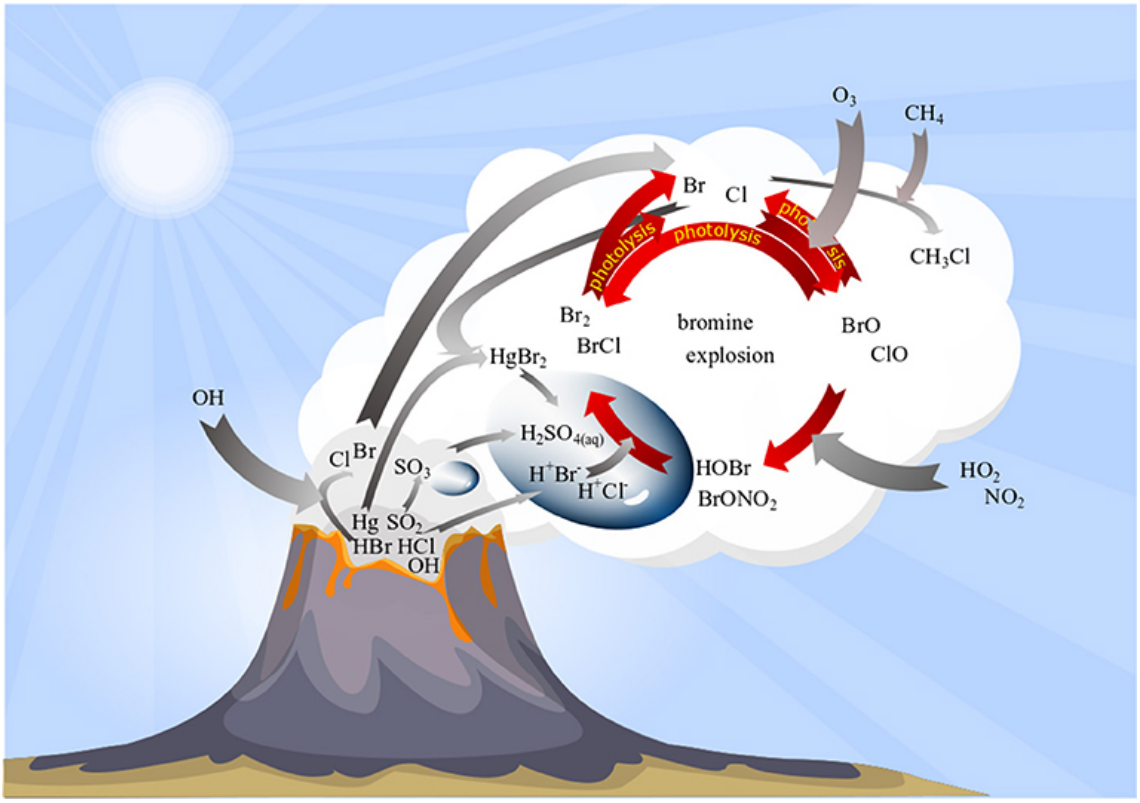

Figure 1.1.1: Overview of the most important chemical processes for bromine chemistry in volcanic plumes (image taken from Gutmann et al. (2018))

.

of Br radicals through OH

$$HBr + OH \rightarrow Br + H_2O. \tag{1.1.1}$$

OH is likely formed in early plume stages. Small amounts of BrO and HOBr emerge from the following two gas phase reactions

$$\begin{aligned} Br + O_3 &\rightarrow BrO + O_2 \\ BrO + HO_2 &\rightarrow HOBr + O_2. \end{aligned} \tag{1.1.2}$$

To achieve high abundances of BrO, heterogeneous reactions are required. Key reactions are the uptake of HOBr and HBr by aerosols to form the volatile Br_2 which after getting released from the aerosol is photolyzed to form Br radicals

$$\begin{aligned} HOBr + H^+_{aq} + Br^-_{aq} &\rightarrow Br_2 + H_2O_{aq} \\ Br_{2(g)} + h\nu &\rightarrow 2Br. \end{aligned} \tag{1.1.3}$$

Each repetition of this cycle doubles BrO concentration and leads to a rapid increase of BrO in the plume.
The high abundance of BrO in volcanic plumes is yet not well understood, especially, since the composition and conditions of volcanic plumes are largely different from conditions in polar regions and salt lakes, where BrO chemistry is studied since many decades.

2 Theoretical Background

In this section the theoretical background for this thesis is given. This includes the basics of radiative transfer in the Earth atmosphere, techniques to monitor atmospheric trace gases via remote sensing, several imaging techniques for trace gas column densities and an introduction to Fabry-Perot interferometers and the IFPICS measurement principle.

2.1 Radiative transfer in the Atmosphere

The most important physical principles used in this work are a direct effect of the interaction of solar radiation with the Earth atmosphere. Theory of radiative transfer or in other words the propagation of electromagnetic waves through a medium consisting of several gas components and particles, for example aerosols, is rather complex. The relevant processes of radiative transfer are discussed in this section and start with elastic scattering processes, called Rayleigh Scattering and Mie Scattering, where photon energy stays constant in the process. Both scattering regimes are distinguished through the size parameter x

$$x = \frac{2\pi r}{\lambda} \tag{2.1.1}$$

where r describes the radius of the collisional partner and the wavelength λ od incoming radiation. Rayleigh scattering occurs for collision partners where the diameter is much smaller compared to the wavelength of the incident light beam, mainly at air molecules. This regime corresponds to a size parameter of $x \ll 1$ and the absorption cross section of Rayleigh Scattering is written in its first approximation as

$$\sigma_R(\lambda) = \approx \sigma_{R0} \cdot \lambda^{-4} \tag{2.1.2}$$

with $\sigma_{R0} = 4.4 \cdot 10^{-16} cm^2 nm^4$ for air **?**.
For the interaction of light with particles having dimensions similar to the incident radiation, resulting in $x \geq 1$, Mie scattering can be described as the emission of coherently excited elementary emitters inside the particle. The main difference compared to Rayleigh scattering is the weak wavelength dependency of the cross section, which is typically in the order of $\lambda^{-1.3}$ Roedel and Wagner (2017), and the preference for the forward scattering direction.
Inelastic scattering processes, with a change in direction and energy of the collision

partner, occur much less frequently. If a molecule changes its vibratio-rotational state of energy, the corresponding scattering process is called Raman Scattering. This phenomenon causes the famous Ring effect, that leas to the filling of Fraunhofer lines of the solar spectrum Grainger and Ring (1962).
Another important effect is the absorption of radiation in the atmosphere. In the microscopic view molecules absorb photons carrying the energy difference $E_p = h\nu(\lambda)$ between two states of excitation of the molecule. The result of this process is a discrete absorption spectrum characteristically for each absorbing species. Macroscopically, the attenuation of radiation in the atmosphere through absorption processes is described by Bouguer-Lambert-Beer‘s law

$$dI(\lambda) = I_0(\lambda) \cdot \sigma(\lambda) \cdot c(l)dl. \tag{2.1.3}$$

Here $I_0(\lambda)$ is the initial radiance and the differential radiance $dI(\lambda)$ is the observed radiance after traversing an infinitesimal atmospheric layer with thickness dl and concentration $c(l)$. $\sigma(\lambda)$ denotes the absorption cross section, which contains the absorption-specific characteristics of the absorbing species. Integration over the light path L yield the optical density $\tau(\lambda)$

$$-ln[(\frac{I(\lambda)}{I_0(\lambda)})] = \sigma(\lambda) \int_0^L c(l)dl = \sigma(\lambda) \cdot S = \tau(\lambda) \tag{2.1.4}$$

with the column density S, which is the integrated amount of particles absorbing along the light path. Rearranging and a generalization for i absorbing species of equation 2.1.4 leads to

$$I(\lambda) = I_0(\lambda) \cdot exp[(-\sum_i \sigma_i(\lambda)S_i)] = I_0(\lambda) \cdot [(-\sum_i .\tau_i(\lambda))] \tag{2.1.5}$$

The last point on the discussion of radiative transfer is the most fundamental. All the processes above occur at the same time when considering a measurement using scattered skylight. Under the assumption of a measurement system looking under a certain field of view (FOV) into a specific viewing direction, incident radiation can be scattered out of the instruments FOV or absorption could take place which reduces the incoming radiance. On the other hand, scattering process from arbitrary directions can increase incident radiation, because of scattering into the instruments FOV. The Radiative Transfer Equation accounts for all this processes

$$\frac{dI(\lambda)}{ds} = -(\tau_A + \tau_S) \cdot I(\lambda) + \tau_S \int_S I'(\lambda, \Omega)\Theta(\Omega)d\Omega. \tag{2.1.6}$$

Here the first term corresponds to Bouguer-Lambert-Beer´s law with an additional term for scattering extinction of Rayleigh and Mie Scattering $\tau_S = \tau_R + \tau_M$. The

second term accounts for scattering processes into the viewing direction, with the intensity $I'(\lambda, \Omega)$ and the scattering phase function $\Theta(\Omega)$. Thermal emission are here excluded as within this thesis only UV scattered skylight is of importance and a more comprehensive discussion is given in **?**.

2.2 Remote sensing in the Atmosphere

Atmospheric remote sensing is an important tool to monitor different trace gases in the atmosphere and allows to draw conclusion from this measurements. In this work only passive remote sensing techniques are discussed which use scattered skylight as a light source instead of artificial light sources. One of the most common techniques in the UV-Vis wavelength range is Differential Optical Absorption spectroscopy (DOAS) which is a dispersive measurement and allows to determine column densities of several trace gases simultaneously **?**. In principle atmospheric extinction through absorption and scattering processes can be described by an extended version of Bouguer-Lambert-Beer's law

$$I(\lambda) = I_0(\lambda) \cdot exp[-\sum_i \sigma_i(\lambda) S_i + \epsilon_R(\lambda) + \epsilon_M(\lambda)] \cdot A(\lambda) \tag{2.2.1}$$

where i runs over the different number of trace gases, ϵ describes the extinction coefficients for Mie and Rayleigh scattering and $A(\lambda)$ characterizes instrumental specific attenuation effects for example through imperfect optical elements. The fundamental principle of the DOAS technique lies in the separation of broadband and high frequency features within recorded spectra to identify the unique narrowband absorption features of the target trace gases. For that purpose the absorption cross sections $\sigma_i(\lambda)$ can be separated as follows

$$\sigma_i(\lambda) = \sigma_{i,broad}(\lambda) + \sigma_{i,narrow}(\lambda). \tag{2.2.2}$$

Inserting this separation into 2.2.1 leads to a split of the intensity into broadband and narrowband parts

$$\begin{aligned} I(\lambda) &= I_0(\lambda) \cdot I_{broad}(\lambda) \cdot I_{narrow} \\ I_{broad} &= exp[-\sum_i \sigma_{i,narrow}(\lambda) S_i + \epsilon_R(\lambda) + \epsilon_M(\lambda)] \cdot A(\lambda) \\ I_{narrow} &= exp[-\sum_i \sigma_{i,narrow}(\lambda) S_i]. \end{aligned} \tag{2.2.3}$$

From that on can define the differential optical density $\tau_{narrow}(\lambda)$ as

$$\tau_{narrow}(\lambda) = -ln\left(\frac{I(\lambda)}{I_{0,broad}(\lambda)}\right) = -\sum_i \sigma_{i,narrow}(\lambda) S_i. \tag{2.2.4}$$

This separation is applicable under the condition of sufficient high spectral information to identify the target trace gases simultaneously. The actual retrieval of the column densities is achieved by fitting literature cross sections $\sigma_{i,narrow}$ to the measured optical densities $\tau_{i,narrow}$ and receive S_i as fit coefficients.

2.3 Trace gas imaging

Imaging of atmospheric trace gases facilitates to monitor spatial distributions of trace gas column densities to retrieve informations about atmospheric composition, chemical processes or turbulence (eg. Louban et al. (2009); Dinger et al. (2018)). As described in the introduction to this thesis, ideally a combination of high tempospatial resolution is necessary to resolve fast chemical processes in the atmosphere on their intrinsic scale. In this section an overview over two common used imaging techniques, Imaging DOAS (IDOAS) and SO_2-cameras is given, including the detection principles and shortcomings that motivated the development of the novel IFPICS technique.
Starting with the IDOAS principle, that combines the dispersive DOAS technique with an imaging setup (e.g. Lohberger et al. (2004)). The DOAS detection principle works as described in section 2.2 but a two dimensional detector is used. To acquire a two dimensional images, scanning is necessary, which can be implemented in two different mechanisms. First, the *whiskbroom* approach where each pixel is scanned sequentially according to a particular scheme, for example line by line. This approach is rather slow. The alternative scanning mechanism is called *pushbroom*, where an image column is recorded and scanning of only several hundreds of columns is necessary. For this approach a 2 dimensional detector is required, where one dimension is used for the spatial information and one dimension for spectral information. This approach is faster than whiskbroom scanning. But looking at the pure photon budget both mechanisms are equally fast Platt et al. (2015). The main advantage of the technique is the simultaneous evaluation of several trace gases combined with a high spatial resolution. Further benefits are the much lower dependence on meteorological conditions, compared to SO_2 cameras as discussed later and no calibration is needed. IDOAS possibly occupy huge storages capacities, because of the three dimensional (two spatial dimensions and one spectral dimension) data. This can be an issue but it depends strongly on the image acquisition speed of the camera. The scanning mechanism often limits temporal resolution and due to that fast dynamical processes cannot be resolved entirely. Additionally, instruments require dispersive and imaging parts which increases instrument volume and complexity which is often not ideal under field conditions.
Another common approach of atmospheric trace gas imaging is realized in SO_2 cameras, which is a non-dispersive imaging technique to monitor SO_2 emission rates from point sources and was first introduced by McElhoe and Conner (1986). This technique relies on the strong SO_2 absorption around $(310 \pm 5)nm$ and uses an UV band-pass filter in front of a two dimensional UV sensitive detector. The filter trans-

mittance is usually called channel A and recording the integrated intensity $T_A(\lambda)$ over this wavelength range enables one to retrieve SO_2 column densities S_{SO_2} as

$$\tau_A = -ln\left(\frac{I_A}{I_{A,0}}\right) = -ln\frac{\int I(\lambda)T_A(\lambda)d\lambda}{\int I_0(\lambda)T_A(\lambda)d\lambda} \propto S_{SO_2} \tag{2.3.1}$$

with the radiance I traversing the trace gas, for example a volcanic plume and the ambient radiance $I_{A,0}$ from a trace gas free sky region in the image or alternatively from an extra image by turning the field of view (FOV) of the instrument to a trace gas free region of the sky. In general detection of SO_2 is possible with this measurement principle. However, the optical density τ_A is not only sensitive to trace gas extinction but also to other extinctions introduced by clouds, aerosol particles or other trace gases. To account for this effect a second filter channel T_B, often called channel B, with a higher central wavelength of $\approx 330nm$ is introduced. In this wavelength region, SO_2 absorption is negligible compared to absorbance in filterband A, but broadband extinctions are mainly constant between the two filter positions. Taking channel B into account, a differential evaluation of optical densities is possible, which corrects for other extinctions as mentioned above. One can calculate the so called apparent absorbance (AA) of the target trace gas as

$$AA = \tau_A - \tau_B = -ln\left(\frac{I_A I_{B,0}}{I_{A,0} I_B}\right) = (\overline{\sigma}_{A,SO_2} - \overline{\sigma}_{B,SO_2}) \cdot S_{SO_2} = k_{SO_2} \cdot S_{SO_2} \tag{2.3.2}$$

with the weighted absorption cross section $\overline{\sigma_{i,SO_2}}$ of SO_2 averaged over the respective wavelength range and the mean weighted absorption cross section k_{SO_2}. The latter parameter can be interpreted as the instrument sensitivity because it describes the effective column density as seen by the instrument. In Figure 2.3.1 SO_2 a plot of the measurement principle of a single and a double filter SO_2 camera setup is shown.

Compared to IDOAS a calibration of the instrument is necessary to determine k_{SO_2}. This can be done in several ways, for example using SO_2 gas cells with known column densities Kantzas et al. (2010) or by a co-aligned DOAS instrument which determines SO_2 column densities at a signal point in the FOV Luebcke et al. (2013). A problem with calibration with gas cells is that even on clear days UV radiative transfer and solar azimuth angle change during the day, which leads to a variation in the incident light behind the plume. This results in different SO_2 sensitivities of the camera Kern et al. (2010). Employing a co-aligned DOAS instrument has the benefits of constantly acquiring spectra, which represents the current illumination conditions and reflects radiative transfer of the scene Kern et al. (2014). Additionally, the measurement is not interrupted by the calibration.
Important benefits of this imaging system are the high spatio-temporal resolution. On the downside, the camera can be used only for sources with high SO_2 abundances and is very sensitive to meteorological influences for example by clouds. Here two

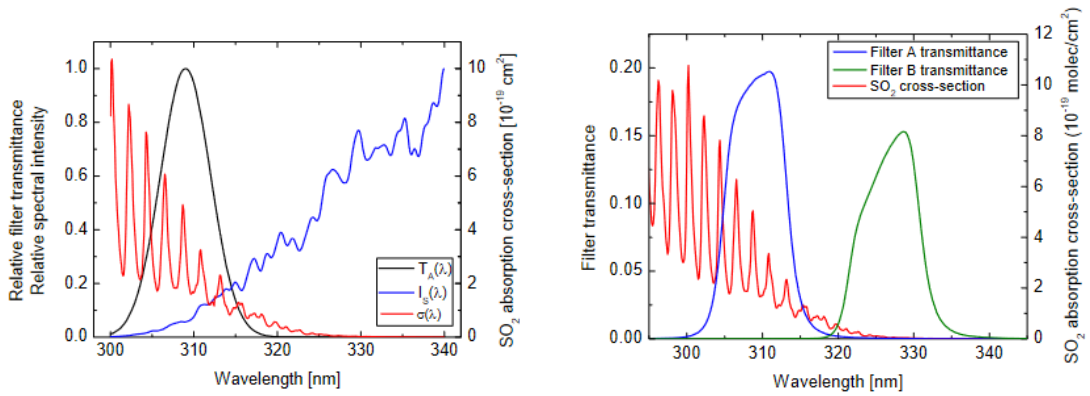

Figure 2.3.1: The left panel shows the the working principle of a single filter SO_2 camera setup. The relative filter transmission T_Δ (black) for filter A, the relative spectral intensity $I_S(\lambda)$ (blue) and the absorption cross section of SO_2 $\sigma(\lambda)$ (red) are plotted against the wavelength. The right panel shows the two filter camera setup with filter A transmittance (blue), filter B transmittance (green) and again the absorption cross section of SO_2 (red).(taken from Kern et al. (2010))

problems occur: First, movement of intensity gradients through the image, introduced for example by a volcanic plume, which introduces false signals, when using only one detector and taking alternating images of the two channels. The other problem is based on radiative transfer. Both wavelength channels have a separation around $20nm$ that can lead to differences in aerosol scattering properties and the assumption of the constant background in the differential evaluation breaks down.

2.4 Fabry-Perot interferometer correlation spectroscopy

Imaging Fabry-Perot interferometer correlation spectroscopy (IFPICS) is a technique that combines the benefits of the IDOAS method and of filter based cameras. For that purpose the bandpass filter of a SO_2 camera is replaced by a Fabry-Perot interferometer (FPI). The transmission spectrum of a FPI can be matched to periodic vibronic absorption structures of a target molecule. Thereby, higher selectivity and sensitivity can be reached (see Kuhn et al. (2014)).
To explain the IFPICS technique, the transmission spectrum of a FPI is derived in the following section according to Demtroeder (2013). The interferometer consists of two plane parallel glass plates with reflective coating (reflectivity R) on the inside and an air filled gap with distance d in between (see Figure 2.4.1). An incident plane wave

$$\mathbf{E} = \mathbf{A_0} \cdot exp[i(wt - \mathbf{kr})] \tag{2.4.1}$$

falling onto to the plane parallel plate under an angle α splits the amplitude A_i into an transmitted and a reflected part. Under the assumption of negligible absorption ($R + T + A \approx R + T \approx 1$) the amplitudes of reflected and transmitted beams are given as

$$\begin{aligned} A_{i,R} &= A_i \cdot \sqrt{R} \\ A_{i,T} &= A_i \cdot \sqrt{1-R} \end{aligned} \tag{2.4.2}$$

resulting in an optical path difference Δs between consecutive reflected or transmitted beams of

$$\Delta s = 2d\sqrt{n^2 - sin^2\alpha}. \tag{2.4.3}$$

with the FPI plate distance d and the refractive index n of the material between the FPI plates. The corresponding phase difference is given for a specific wavelength λ of the incoming beam as

$$\Delta\phi = \frac{2\pi\Delta s}{\lambda + \delta\phi}. \tag{2.4.4}$$

$\delta\phi$ is introduced to account for phase jumps. The total amplitude of transmitted beams is given by the sum over all partial beams which leads to an intensity profile of

$$I_T = I_0 \cdot \frac{(1-R)^2}{(1-R)^2 + 4R \cdot sin^2(\Delta\phi/2)}. \tag{2.4.5}$$

Introducing the abbreviation $F = \frac{4R}{(1-R)^2}$ yields the Airy-Formula for transmitted beams

$$I_T = I_0 \frac{1}{1 + Fsin^2(\Delta\phi/2)}. \tag{2.4.6}$$

Finally, the FPI transmittance T_{FPI} is calculated as

$$T_{FPI} = \frac{I_T}{I_0} = \frac{1}{1 + Fsin^2(\Delta\phi/2)} \tag{2.4.7}$$

which is extensively used in this work.

As shown in Figure 2.4.1 the FPI is implemented in a parallel beam path in the optical setup. Imagine an extended light source in the focal plane of L_1, the emitted

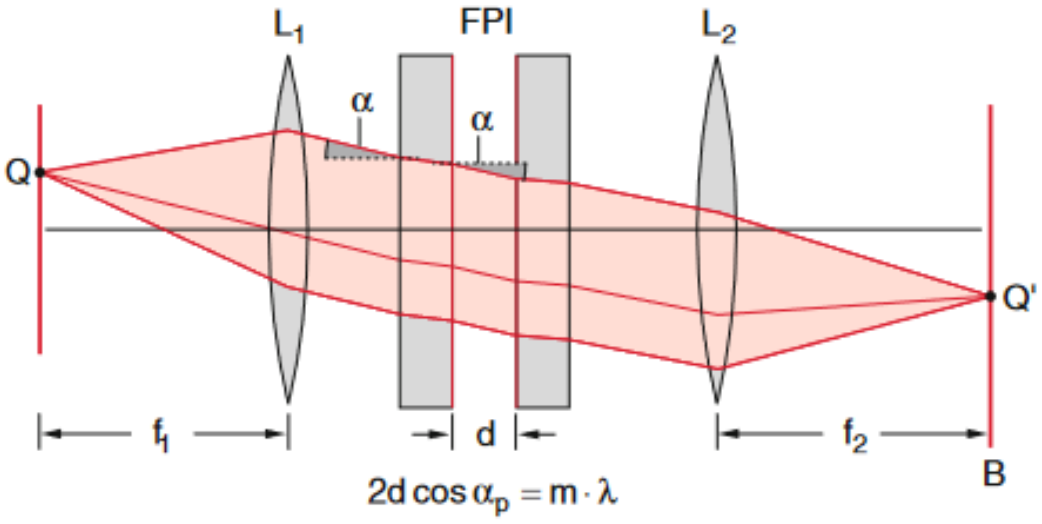

Figure 2.4.1: Example of an optical setup for a FPI imaging instrument (image taken from Demtroeder (2013))

light passes parallel through the FPI under incidence angle α. Positive interference occurs for angles which obey

$$\Delta s = 2d\sqrt{n^2 - sin^2(\alpha)} = 2dcos(\alpha) = m \cdot \lambda \tag{2.4.8}$$

with an integer m. For monochromatic light sources, a pattern of bright rings depending on the total Finesse of the FPI could be observed. The Finesse is defined as the ratio of the free spectral range (FSR) and the full width at half maximum of the transmission peaks.

In Figure 2.4.2 a sketch of different FPI parameters and their influence on the transmission spectrum $T_{FPI}(\lambda)$ is shown. The FPI peaks are characterized by the FSR, $\Delta\lambda$ and their full width at half maximum (FWHM) $\delta\lambda$.

2.4.1 Trace gas detection by IFPICS

Trace gas detection by IFPICS uses a similar approach as SO_2-cameras. By recording optical densities in two spectral channels the differential optical density can be determined (see section 2.3).

Similar to SO_2 camera measurements the difference between an on-band and an off-band optical density of the target trace gas is used. The FPI is matched to the trace gas absorption spectrum by choosing appropriate physical parameters (see Figure 2.4.3). The periodicity of the FPI transmission is matched to the trace gas absorption structure via the plate separation d. Through an assessment of the signal to noise ratio the optimum finesse of the FPI can be found. In addition, a bandpass filter is used to isolate a spectral range, where the correlation of FPI transmission

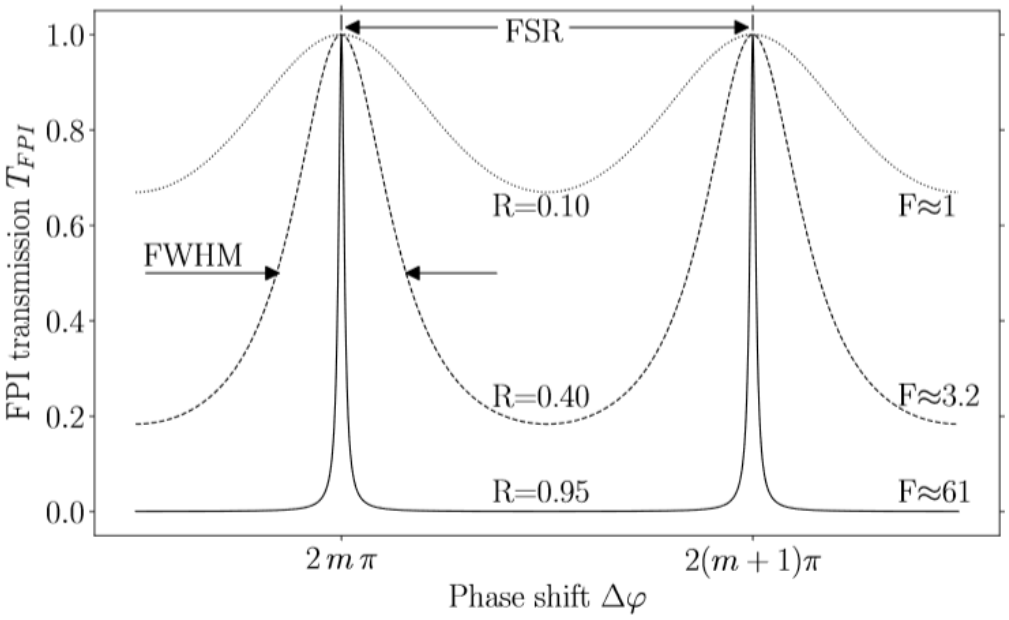

Figure 2.4.2: FPI transmittance T_{FPI} in dependence of the phase shift $\Delta\phi$ is drawn for different reflectivities R. The Finesse F is defined as the ratio of the free spectral range (FSR) and the full width at half maximum (FWHM) od the transmission peaks. (image taken from Fuchs (2019)).

and trace gas absoption is highest. The procedure is described in detail in Kuhn et al. (2014), Kuhn et al. (2019) and Fuchs (2019). In this thesis an available FPI is used, that was matched to BrO absorption at around $340nm$ according to Kuhn et al. (2019). The apparent absorbance of the target trace gas is calculated, similarly to the SO_2 camera (see equation 2.3.2) using the differential optical densities for the on-band $\tau_{FPI,on}$ and off-band $\tau_{FPI,off}$ position. A calibration further yields trace gas column densities S

$$AA_{FPI} = \tau_{FPI,on} - \tau_{FPI,off} = k_{FPI} \cdot S \tag{2.4.9}$$

with the instrument sensitivity k_{FPI}. Calibration can be done analogously to calibration of the SO_2-camera, by measuring gas cells with known trace gas concentrations or by using a parallel DOAS measurement. Additionally, an instrument model can be used to calculate calibration curves from the known filter and FPI transmissions and the known trace gas absorption spectrum.
Imaging of gas cells is not practical for BrO calibration, as it cannot be handled in gas cells due to its self reactivity. In this thesis a combination of HCHO gas cell and a DOAS measurement is used.
Through the periodic transmission features of the FPI, a high selectivity can be achieved and the benefits of fast image acquisition through the non dispersive approach are retained. This technique can be applied to several trace gases for example

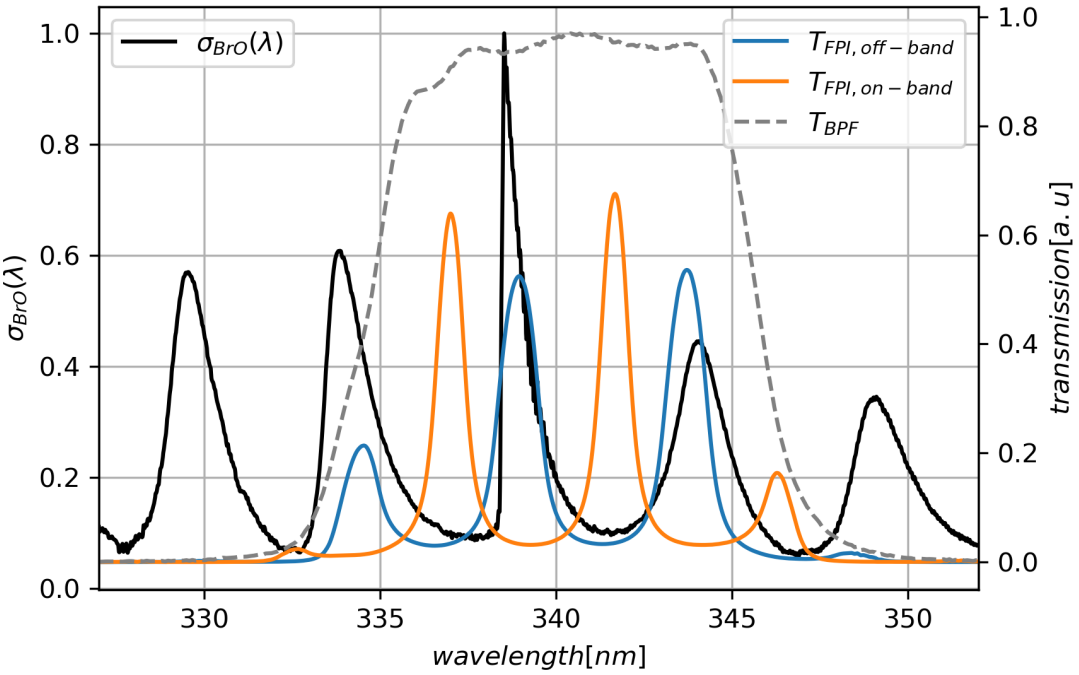

Figure 2.4.3: Detection principle of IFPICS instrument. The orange line shows the FPI transmission spectrum $T_{FPI,A}$ in on-band setting, the blue line the FPI transmission $T_{FPI,B}$ in off-band setting, the black line the absorption cross section σ_{BrO} of BrO and the grey dotted line the chosen wavelength range by a bandpass filter transmission T_{BPF}.

SO_2, BrO, HCHO, OClO or NO_2 (see Fuchs et al. (2021), Kuhn et al. (2019)). Compared to IDOAS, the IFPICS technique reduced spectral information to two trace gas specific spectral channels, while allowing full frame imaging, has the potential to provide faster measurements of reactive trace gases e.g. to study their chemical dynamics. The optical infrastructure is also reduced, what makes field recordings much easier.

2.4.2 The IFPICS instrument model

A numerical model based on the FPI transmission, literature cross section and a solar atlas spectrum is used to investigate the ideal measurement parameters by determining the theoretical maximum AA and the corresponding incidence angles on the FPI as well as an investigation of cross interferences. The discussion is based on Fuchs (2019), Kuhn et al. (2019) and Fuchs et al. (2021).
Modelling of the AA is performed by inferring the incident radiation I_0 from a high resolution top of the atmosphere (TOA) solar atlas spectrum $I_{0,TOA}$ according to Chance and Kurucz (2010). The TOA solar spectrum is scaled according to

a Rayleigh scattering atmosphere with a scaling factor of λ^{-4} and additionally a correction for stratospheric Ozone (O_3) is applied leading to a scattered skylight radiance $I_0(\lambda)$ of

$$I_0(\lambda) = I_{0,TOA} \cdot e^{-\sigma_{O_3}(\lambda)\cdot S_{O_3}} \cdot f(\lambda^{-4}). \tag{2.4.10}$$

The O_3 correction is introduced by a Lambert-Beer term with the absorption cross section σ_{O_3}. On the basis of I_0, radiances seen by the instrument can be determined for the respective wavelength channel. For that, the instrument transfer function $T_{instr,i}(\lambda)$ has to be considered given by

$$T_{instr,i}(\lambda) = T^{eff}_{FPI,i}(\lambda) T_{BPF}(\lambda) Q(\lambda) \eta(\lambda) \tag{2.4.11}$$

with the measured band-pass filter transmission $T_{BPF}(\lambda)$, the quantum efficiency of the detector $Q(\lambda)$ and a spectral loss factor $\eta(\lambda)$ from the optical components of the instrument. The effective FPI transmission $T^{eff}_{FPI,i}(\lambda)$ describes the real beam configuration incident on the FPI. Beams incident on the FPI are assumed to have a cone shape. Following this assumption the incident angles α_i are distributed over an angle range $\gamma(\alpha_i, \omega_c, \theta, \phi)$ where θ and ϕ describe the normal polar and azimuth angle and ω_c the half cone opening angle of the light beams. Due to that, the single beam FPI transmission $T_{FPI,i}$ calculated as

$$T_{FPI,i}(\lambda; \alpha_i, d, n, R) = \Big[1 + \frac{4R}{1-R^2} sin^2\Big(\frac{2\pi n d cos\alpha_i}{\lambda}\Big)\Big]^{-1} \tag{2.4.12}$$

is expanded by a weighted average over the corresponding angle range as

$$T^{eff}_{FPI,i}(\lambda; \gamma(\alpha_i, \omega_c,), d, n, R) = \frac{1}{N(\gamma(\alpha_i, \omega_c))} \int_0^{\phi_{max}} \int_{\theta_{min}}^{\theta_{max}} T_{FPI,i}(\lambda; \gamma\alpha_i, \omega_c, \theta, \phi, d, n, R) sin\theta d\theta d\phi. \tag{2.4.13}$$

$N(\gamma(\alpha_i, \omega_c))$ is the normalization factor for the cone integration. Using the full divergent beam model to describe the FPI transmission decreases the effective Finesse of the FPI leading to a blurring effect of the FPI fringes. From this calculation the spectrally integrated radiance $I_{FPI}(\alpha)$ seen be each detector pixel is given as

$$I_{FPI}(\alpha) = \int_\lambda I_0(\lambda) e^{-\sum_i \sigma_i(\lambda)\cdot S_i} T_{instr,\alpha}(\lambda) d\lambda \tag{2.4.14}$$

and the optical density $\tau_{FPI}(\lambda)$ can be calculated as

$$\tau_{FPI}(\alpha) = -ln\Big[\frac{I_{FPI}(\alpha)}{I_{0,FPI}(\alpha)}\Big] \quad = -ln\Big[\frac{\int_\lambda I_0(\lambda) e^{-\sum_i \sigma_i(\lambda)\cdot S_i} T_{instr,\alpha}(\lambda) d\lambda}{\int_\lambda I_0(\lambda) T_{instr,\alpha}(\lambda) d\lambda}\Big] \tag{2.4.15}$$

which is now a function of the incidence angle and the absorbing species i. From this result the AA_{FPI} can be determined for the incidence angles $\alpha_{A,B}$ which are independent until a maximum $AA_{FPI,max}$ is reached

$$AA_{FPI} \stackrel{!}{=} AA_{FPI,max} = \tau_{FPI}(\alpha_A) - \tau_{FPI}(\alpha_B) = \tau_{FPI,A} - \tau_{FPI,B} = k_{max} \cdot S. \quad (2.4.16)$$

This result give the operating settings of the FPI yielding the highest correlation with the absorption structures of the target trace gas i and due to that the maximum sensitivity k_{max}. Because of the independent integrations in the numerator and denominator in Equation 2.4.15, the proportionality $\tau \propto S$ does not hold any more and $k \neq const$ yields $AA_{FPI} \not\propto S$. However, a double linearization of 2.4.15 is possible, under the assumption of $\sigma \cdot S \ll 1$. Proportionality between $AA_{FPI} \propto S$ can be recovered from this assumption. A detailed calculation is given in Fuchs (2019).
The described model allows to characterise and calibrate IFPICS instruments. Model studies for HCHO and BrO instruments are introduced in section 5.1.

3 The IFPICS Instrument

In this section, the IFPICS instrument is described, particularly focussing on developments since Fuchs et al. (2021). In Figure 3.0.1 an image of the IFPICS instrument is shown as well as a sketch of the optical setup of te camera. A short presentation of the major compounds, FPI and detector, is followed by a detailed description of the optical setup. Major developments of the instrument compared to Fuchs (2019) and Fuchs et al. (2021) are a new detector, a redesigned optical setup around lens system 2 and a newly developed measurement software.

3.1 The Fabry-Perot-Interferometer

In this section, a short technical description of the FPI used in the IFPICS instrument is given. The interferometer used in this setup is provided by *SLS Optics Ltd* and has the same housing dimensions as presented in Fuchs (2019). Images of the FPI can be found in Figure 3.1.1.

A theoretical description of the working principle is given in section 2.4. The FPI has a clear aperture of $CA_{FPI} = 20mm$ and its transmission is fitted to the absorption structures of BrO at a wavelength of $(340\pm5)nm$ resulting in the following parameters. The plate distance is $d = (12.330 \pm 0.100)\mu m$. The etalon is filled with air with refractive indices of $n_{BrO,air} = 1.0029$ for air and $n_{BrO,glass} = 1.4792$ for glass Polyanskiy (2021). The inner surfaces have a reflective coating with a reflectivity of $R_{BrO} = 0.70$. The outer surfaces are anti-reflex coated and inclined by $\epsilon = 0.5$ to prevent the formation of further etalon structures. A sketch of the FPI setup can be found in Figure 3.1.2.

3.2 The Imaging Detector

Throughout this thesis two different detectors were used. Both cameras are based on the sCMOS technology and have a resolution of 4 MP. Differences occur in the quantum efficiency, dimensions and temperature stabilisation. The first and now outdated imaging detector applied in the IFPICS instrument was the SCM2020-UV camera provided by *EHD imaging GmbH*. The camera uses the UV sensitive $1.2''$ sensor GSENSE2020-BSI as detector which has a quantum efficiency of 33% to 40% between $300nm - 350nm$. The detector was used in Fuchs (2019) and Fuchs et al. (2021) as well as during the first parts of this thesis. Several issues in particular regarding the image acquisition speed, cooling, and software usability lead to the decision to update the detector for the BrO camera.

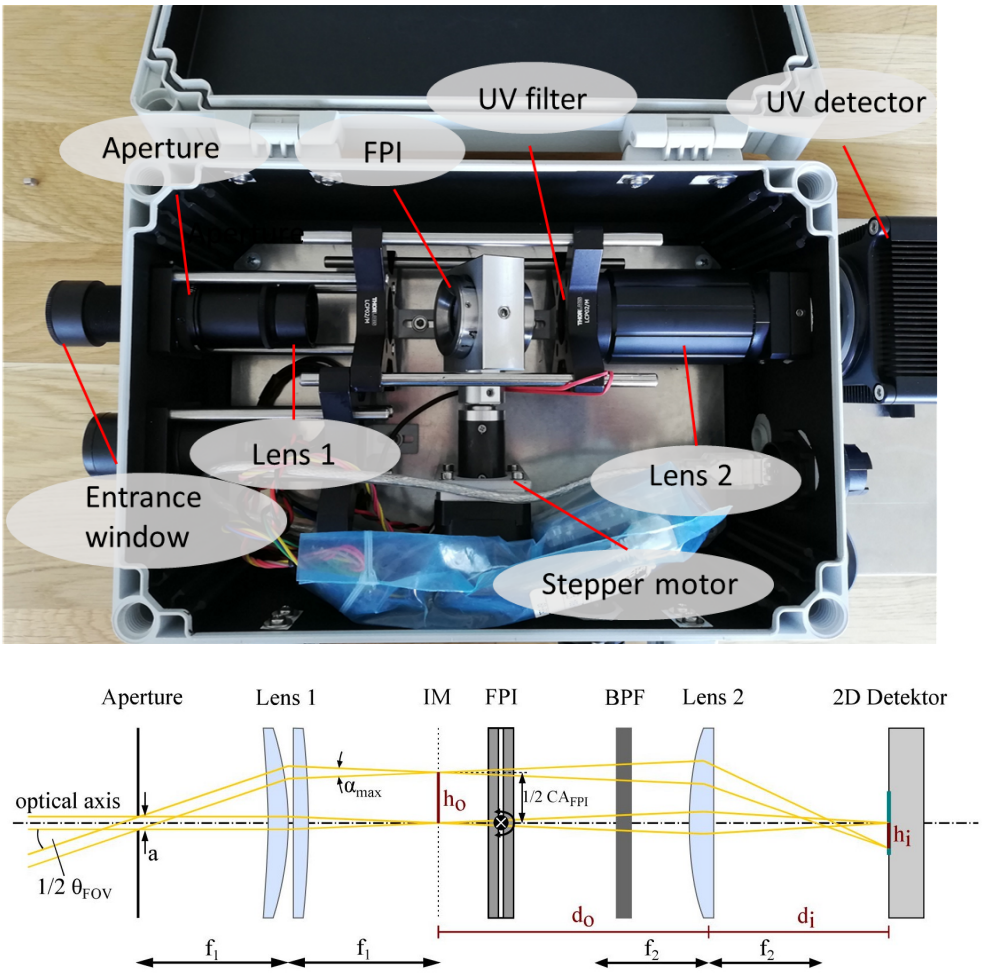

Figure 3.0.1: The upper panel shows an image of the IFPICS instrument including descriptions of the main components. The lower panel shows a sketch of the optical setup shown in the upper panel. Θ_{FOV} is the opening angle of the camera,α_max the divergence angle of the incoming light beams, the focal length of the lens systems are called f_1 and f_2, the clear aperture of the FPI is abbreviated as CA_{FPI} and the object distance and image distance are given as d_o and d_i (taken from Fuchs (2019))

.

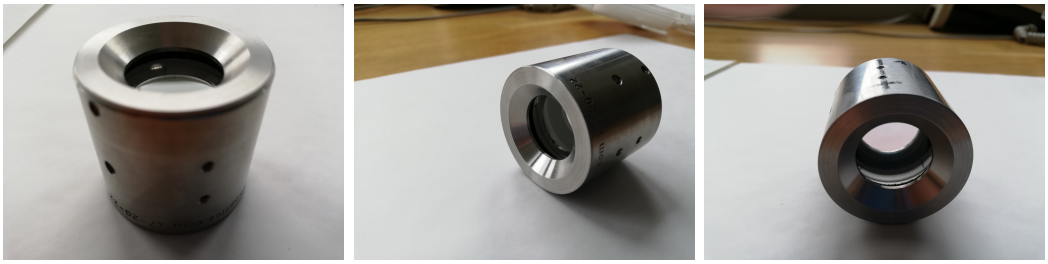

Figure 3.1.1: Images of FPI. The etalon is covered in a steel reel with an outer diameter of $38mm$, $34.5mm$ length and a clear aperture of $20mm$.

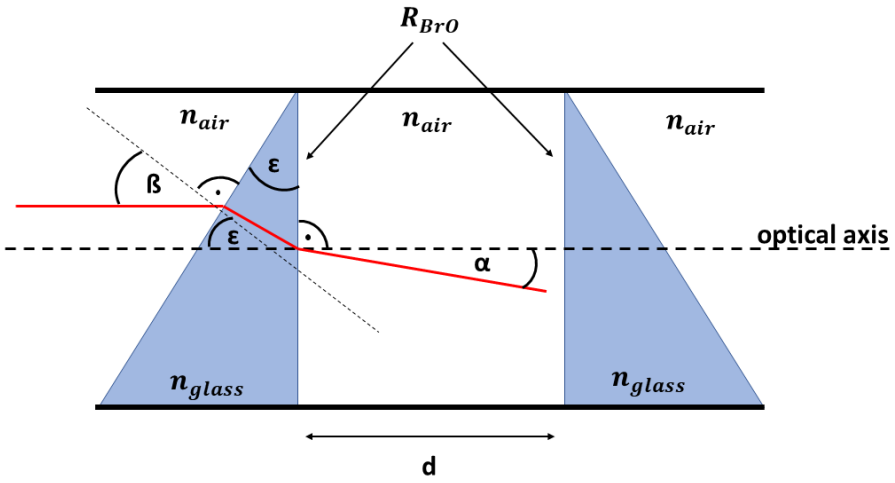

Figure 3.1.2: Sketch of realistic FPI setup including an exemplary beam path. All dimensions are overstated for viewing reasons. β describes the angle of incidence on the etalon, α shows the beam angle inside the etalon and ϵ describes the wedge angle of the FPI. The refractive indices are abbreviated as n_{air} and n_glass for air and glass. R_{BrO} is the reflectivity and d the plate distance of the FPI.

The updated camera pco.edge 4.2 bi UV is provided by *PCO AG*. The detector is a back illuminated scientific CMOS (bi sCMOS) sensor with a pixelsize of $6.5\mu m \times 6.5\mu m$ and dimensions of $13.3mm \times 13.3mm$. Furthermore the camera is coolable up to $-25°C$ by a build in peltier-element and heat sink. This results in a stable dark current required under field conditions.The camera is connected via an USB 3.1 Gen 1 connector and has a typical power consumption of $4.5W$ over USB and $10W$ over the power connector, however this depends strongly on environmental conditions and the selected cooling point.

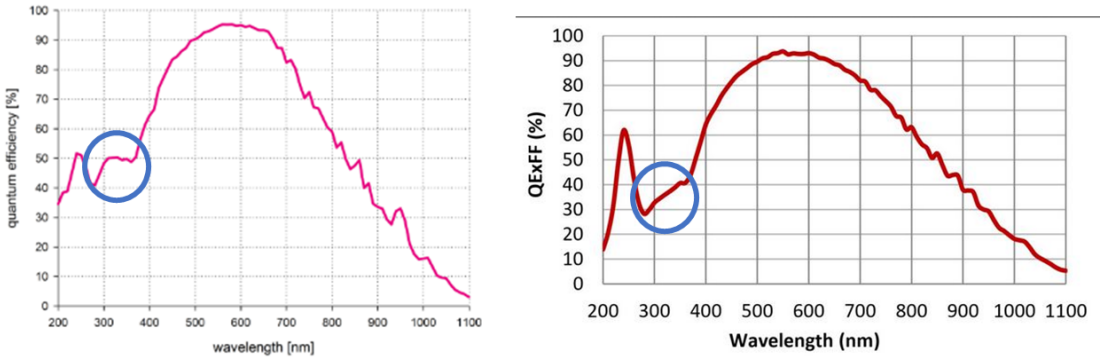

Figure 3.2.1: Quantum efficiency the of pco.edge 4.2 bi UV (left) and the SCM2020-UV (right) camera sensors. The blue circle marks the wavelength range important for this work (taken from the detector data sheets (AG (2021), ehd imaging GmbH (2021))

From Figure 3.2.1 one can obtain a quantum efficiency in the wavelength range between $300nm - 350nm$ of 48% to 50% which will be significantly higher compared to the previous detector. A detailed comparison of both detectors can be found in Table 3.1.

Parameter	SCM2020-UV	pco.edge 4.4 bi UV
sensor size [mm]	13.3 x 13.3	13.3 x 13.3
pixel size [μm]	6.5 x 6.5	6.5 x 6.5
resolution [HxV]	2048 x 2048	2048 x 2048
amplifier gain	x1.5 (low) x10.5 (high)	not specified
conversion factor [signal/eˆ-]	0.0718 (low) 2.2 (high)	0.8
full well depth [keˆ-]	54 (low) 1.8 (high)	48
dark current [eˆ-/s/pix]	25 (high)	0.2
read out noise [eˆ-]	23 (low) 1.6 (high)	1.9
exposure time [s]	10ˆ{-4} - 1000	10ˆ{-6} - 20
max frame rate [fps]	45	40
power supply	5 V DC via USB3.0	USB 3.1 Gen1 and power connector (24 V DC)
dimensions (WxHxD) [mm]	68 x 68 x 43.5	85 x 80 x 99

Table 3.1: Comparison of both detectors. High and low refer to the high and low gain image settings of both detectors. The high gain settings will not be used for this thesis.

3.3 Optical setup

The dimensioning of the optics setup is based on calculations of Kuhn et al. (2019) and was built by Fuchs (2019). The FPI is implemented in a 1″ optical construction as shown in the lower panel of Figure 3.0.1. To ensure all pixels of the detector see the same FPI transmission the interferometer must be placed in a parallel beam of the telecentric optics. In this configuration the FPI sits in a parallel beam section of the instrument and FPI tuning for all pixels in two tilt settings is easy. Tuning of the FPI is achieved through altering of the incidence angle on the FPI. For that purpose the FPI is mounted on a stepper motor. An alternative setup with a FPI in a divergent beam yields a higher light throughput but tuning is rather difficult (see Kuhn et al. (2014)). The first part of the optics, which consists of aperture and lens system 1, parallelizes the incoming light beam. To reduce spherical aberration effects the first lens consists of two lenses, first a positive meniscus lens with a focal length of $f_{pm} = 100mm$ and second a plano-convex lens with a focal length of $f_{pc} = 100mm$ yielding a total focal length for the lens system of $f_{tot,1} = (\frac{1}{f_{pm}} + \frac{1}{f_{pc}})^{-1} \approx 50mm$. This calculation is correct for the visible wavelength range but in the UV the focal length of the lens system is shorter around $f_{UV,1} \approx 47mm$. The field of view (FOV) Θ_{FOV} of the instrument is given by the focal length $f_{tot,1}$ of the first lens system and the clear aperture CA_{FPI} of the FPI through

$$\Theta_{FOV} = 2 \cdot arctan\left(\frac{1/2CA_{FPI}}{f_{tot,1}}\right) \approx 17^{\circ} \tag{3.3.1}$$

with $CA_{FPI} = 15mm$ instead of $20mm$, because of tilting. Parallelization of the light beams has a lower limit due to the finite aperture opening and can be quantified through a maximum divergence angle α_{max} which is determined by the aperture and the focal length of lens sytem 1. α_max is limited through the incidence angle dependence of the FPI's transmission spectrum. For FPIs with specifications as in this thesis α_max is in the range of one degree (see Kuhn et al. (2014) and Fuchs (2019).

$$\frac{\alpha_{max}}{2} = arctan\left(\frac{1/2a}{f_{tot,1}}\right). \tag{3.3.2}$$

From the assessment in 3.3.2 one can calculate a maximum diameter of the aperture under the condition of $\alpha_{max} = 1°$ as

$$a_{max} = 2 \cdot tan\left(\frac{\alpha_{max}}{2}\right) \cdot f_{tot,1} = 0.87mm. \tag{3.3.3}$$

The new camera setup uses also two lenses for lens 2, however, in opposite order than lens 1. Thereby the incidence angles on the glass surfaces and thereby the spherical aberration is minimized (see Figure 3.3.1).

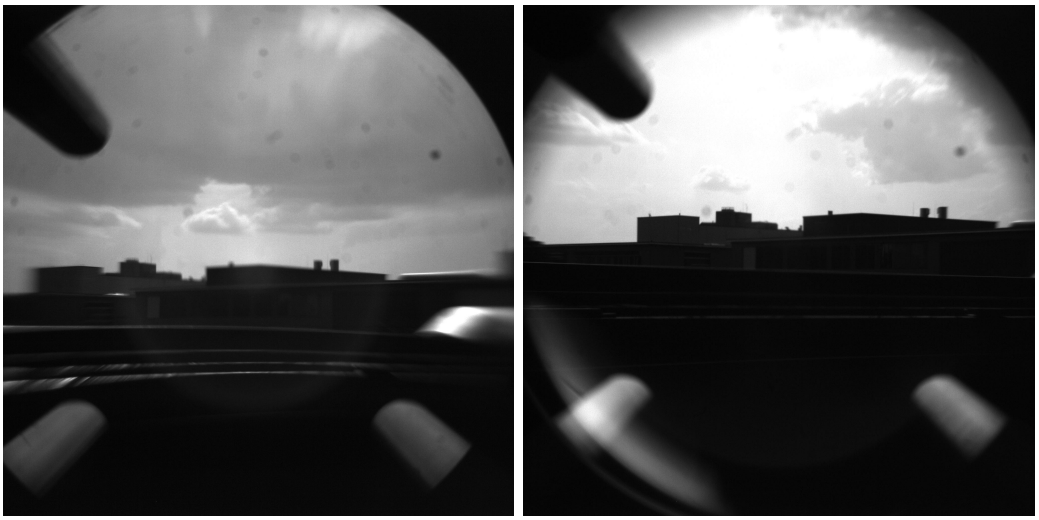

Figure 3.3.1: Comparison of a single (left panel) and a double (right panel) lens system for lens 2. Images were taken in an experimental setup. Images of the opposing building of the laboratory are taken to judge image quality. Lens aberrations are strongly reduced in the right image.

The improvements are visible, lens aberrations towards the corners of the image are drastically reduced in the two lens version on the right hand side. The images were taken in an experimental optical setup and without the FPI to achieve a higher light throughput. The FPI should not change anything regarding the focus point of

the camera, because it will be introduced in the telecentric part of the optics. The focussing process will be described in the following part.
The beam divergence leads to an imaginary image (IM) which is mapped onto the detector by the second lens pair. Both, the distances d_o between IM and lens 2 and d_i between lens 2 and detector are adjustable, see Figure 3.0.1, for the following reasons. First, according to the lens equation the magnification of the IM could be adjusted, which will be the first step before focussing the camera. A calculation of this effect is presented in Fuchs (2019). The magnification factor in this setup will be close to unity but one can introduce an optical binning effect by scaling the image size smaller than the detector dimension which increases radiance on a smaller detector area. This principle can be used in low light conditions. The image size on the detector can be tuned by changing the distance between detector and lens system 2. Second, the focus of the camera is set by changing the distance d_0. For this process a new tube was implemented that ensures a smooth movement of the lenses and the detector which is mounted on a rail system and can be fixed after focussing. The goal of this process is to focus the total optical setup towards infinity.

3.4 The IFPICS instrument characterization

In the following section a complete characterization of the IFPICS instrument will be performed including a characterization of the FPI in the instrumental setup. Additionally, a angle to step calibration of the stepper motor has been done. For this measurements the 2D detector will be interchanged by an optical fibre mount and the instrument will be connected to an AvaSpec-ULS2048 spectrograph build by *Avantes*. As a light source a xenon arc lamp is used, which has the benefit of a rather constant output compared to skylight for example, which can change over the period of the measurement. In this configuration one can determine all FPI parameters and characterize the angle dependence of the stepper motor. The measurements will follow the description in Fuchs (2019).

3.4.1 Wedge angle alignment

The FPI consists of two glass plates which have a plane parallel inner surface and the outer surfaces are inclined with a wedge angle of $\epsilon \approx 0.5°$ as indicated in Figure 3.1.2. Aligning the wedge angles of the FPI is very important. Correct alignment will be reached when the wedged surface is vertically aligned in the camera setup. This procedure ensures a constant angle calibration and is necessary for the reproducibility of the measurements.
The FPI will be rotated with respect to the optical axis starting at an arbitrary point. Through the rotation a shift in the incidence angle α will be enforced which leads to shift in the transmission spectrum. Here two scenarios have to be distinguished. First the incoming beam has an incidence angle parallel to the wedge angle. This will not result in a change of the incidence angle because the orthonormal of

the wedged surface will rotate around the incoming beam. In the second scenario the incoming light beam is not parallel to the optical axis of the FPI. Now, rotation leads to an oscillation of incidence angle with an amplitude of two times the wedge angle. Because the transmission spectrum is a function of the cosine of incidence angle the shifts in transmission spectra are small, but one can amplificate the shift by introducing a bias angle by tilting the FPI prior to the measurement. The FPI has been tilted to an angle of $\approx 15°$. The transmission spectrum with maximal shift corresponds to the correct wedge angle alignment in bias angle direction. Then, a first measurement round has been performed with large angle steps of 90° for a loose determination of the correct alignment position. Afterwards, a second precise run has been performed with a higher angular resolution of 10°. The correct alignment resulting from this measurement has been marked on the FPI. The corresponding spectra can be found in Figure 3.4.1.

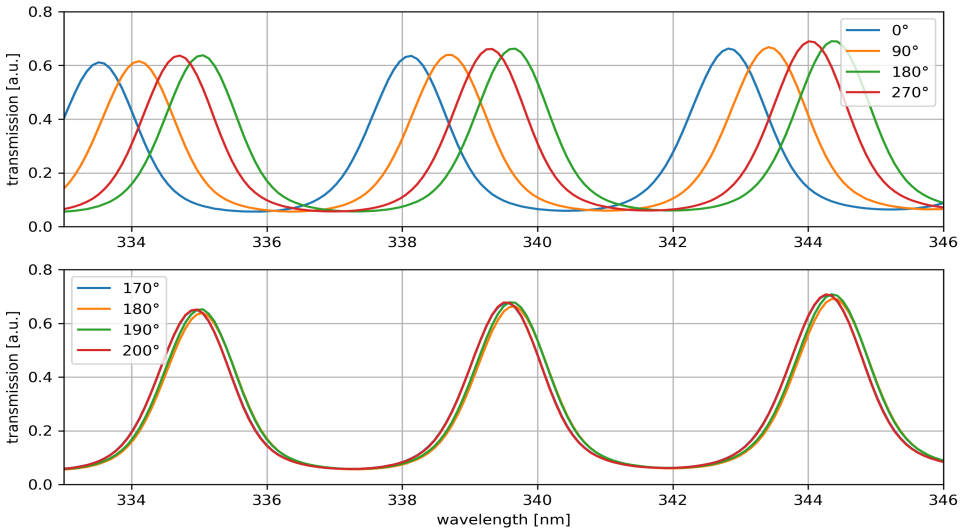

Figure 3.4.1: FPI transmission spectra for different rotation angles starting at an arbitrary point. upper panel: approximate angle determination lower panel: precise determination

3.4.2 Zero position

The zero-position of the FPI is the corresponding angle position where the transmitted beams inside the etalon have a inclination of zero degrees, which equals to $\alpha = 0°$, following 3.1.2. The measured zero position will be the starting point for a tilt angle to motor step calibration of the camera and is essential for choosing the correct angles to compare the FPI model with measurements. The stepper motor has a resolution of $6.25° \times 10^{-3}$, which corresponds to a turn of 90° in 14400 steps.

The measurement principle is very similar to the wedge angle alignment. The FPI will be build into the setup in correct wedge angle alignment. Scanning a large motor step range and determining the step position with maximum shift to higher wavelength gives the correct zero position. Due to the cosine dependency of the incidence angle shift in transmission spectra gets smaller towards the zero position. The corresponding measurement can be found in Figure 3.4.2.

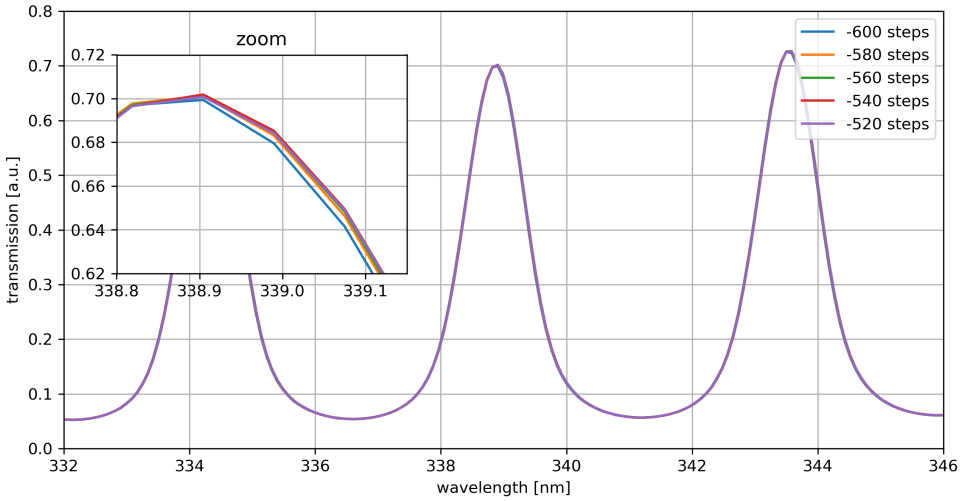

Figure 3.4.2: Measurement to determine the zero-position of the FPI. The upper left panel shows a zoom into the middle peak to illustrate the small spectrum shift due to the cosine dependency on the incidence angle.

For the BrO-FPI one obtains a zero position of

$$BrO - FPI : p_{0^\circ} = (530 \pm 10)\mu - steps. \tag{3.4.1}$$

3.4.3 Plate distance

The plate distance of the FPI is an important model parameter but the manufacturers value is not precise enough. Due to that an additional measurement has to be performed on the plate distance.
To determine the precise value of the plate distance a FPI transmission spectrum in the zeros position and correct wedge angle alignment will be compared to a modelled spectrum with an incidence angle of 0°. Following this approach the only free model parameter remaining is the plate distance. Varying this parameter until the measured and modelled spectra match gives the correct plate distance of

$$d_{FPI,BrO} = (12.366 \pm 0.002)\mu m \tag{3.4.2}$$

which lies well in the manufactures range of $(12.330 \pm 0.100)\mu m$. The measurement is shown in Figure 3.4.3.

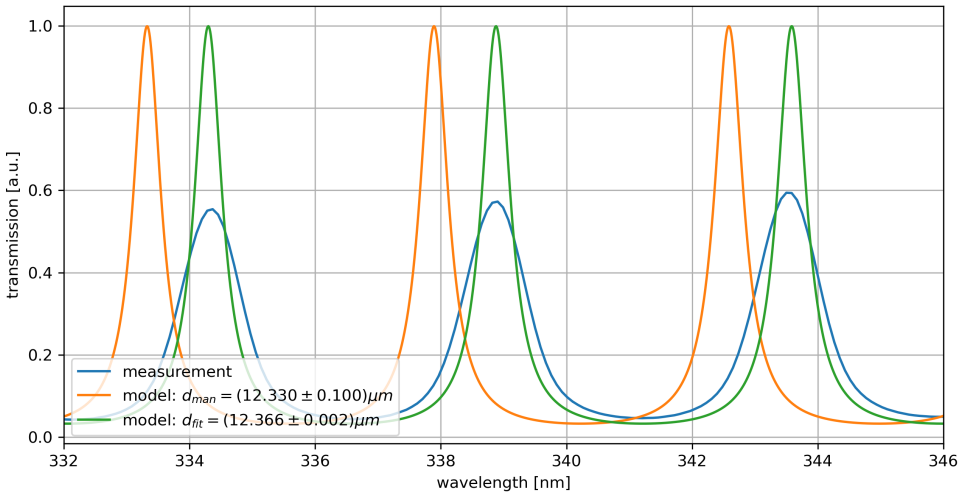

Figure 3.4.3: Measurement of the plate distance by fitting the model to the FPI transmission spectrum in zero-position.

3.4.4 Angle calibration

For the step to angle calibration of the stepper motor one can start at the zero position and move the stepper in distinct steps and check if the modelled spectrum with a calculated angle matches the measured spectrum for the corresponding step width.

The corresponding measurement can be found in Figure 3.4.4. Here the exemplary calibration between stepper motor and actual angle steps will be shown. The modelled spectra match nice the expected transmission spectrum from the measurement. Important for our purposes is that the calibration fits well in the measurement wavelength range around $340nm$. Deviations between model and measurement are expected towards higher tilt angle because of the non linear dependence between transmission maxima and wavelength and towards higher wavelengths, because the free spectral range of the FPI is only constant to first order. Another way of calibrating the instrument is shown using imaging measurements is shown in section 5.2.1.

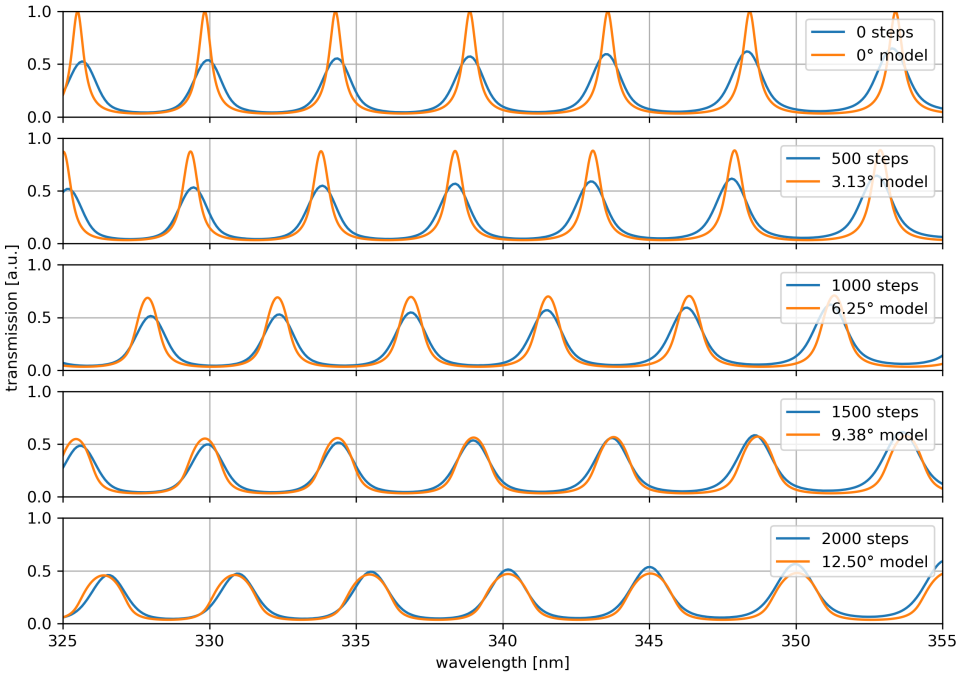

Figure 3.4.4: Measurement of the angle calibration. The blue line corresponds to the measured FPI transmission spectrum for a certain motor position in steps. The orange line will be the simulated transmission spectrum with the calculated angle.

4 The IFPICS data evaluation

In the following sections the data evaluation process of IFPICS images is discussed. A general goal of this process is to evaluate differential optical densities to yield the two dimensional column density distribution of the target trace gas as described in section 2.4.1. For that purpose, the two measurement images (on-band image and off-band image) go through different correction and processing steps, starting with a dark current correction. Here a dark image, that was taken before the measurement is subtracted from the measurement image to correct for the dark signal and the offset of the analogue to digital converter (ADC). A detailed description is given in section 4.2. The next correction step is a flat field correction. For that purpose images of the clear sky are taken and the measurement images are divided by this flat images to correct for pixel to pixel non uniformities, vignetting effects and dust on the optical instrumentation (see 4.4). In addition, several averaging processes are performed to achieve the highest possible signal to noise ratio (SNR) and a low detection limit, including optical flow calculations and a high pass filter correction.

4.1 Linear camera model and noise sources

To start the evaluation process a brief discussion on different noise sources is given based on the european machine vision association (EMVA) 1288 standard Association (2021), which is only valid for cameras described by a linear camera model. A linear camera model describes an ideal sensor and enforces the following assumptions. The strongest assumption is the linearity of the sensor, meaning the digital signal μ increases linearly with the received amount of photons. The mean photon number μ_p hitting a detector pixel with area A during the exposure time t_{exp} is given as

$$\mu_p = \frac{AEt_{exp}}{h\nu} \tag{4.1.1}$$

with the irradiance E, the Planck constant h and the photon frequency ν . The accumulated charge units get converted through an ADC into a digital signal μ_y in a linear manner

$$\mu_y = \mu_{y,dark} + K\mu_e \tag{4.1.2}$$

with the mean dark signal $\mu_{y,dark} = K\mu_d$. μ_d describes the mean number of electrons present without any light hitting the detector, because of thermal generation

of charge units the dark signal roughly increases exponential with temperature. The linear camera model is described by the overall system gain K in digits per electrons (DN/e^-). In this work the term digital units and counts are used equivalent. Summing up, one gets a linear equation for the mean grey value of a detector pixel as

$$\mu_y = \mu_{y,dark} + \frac{\eta K A}{h\nu} t_{exp} \tag{4.1.3}$$

where η describes the quantum efficiency of the detector, the wavelength depending ratio of the mean photon number hitting the detector and the resulting mean number of charge units. Several other assumptions including the independence of different noise sources and their statistical invariance in space and time can be read up in Association (2021). Next, a brief discussion on noise sources and their description in the linear camera model is given.
Shot noise is characterized through statistical fluctuations of charge units. Following the quantum mechanical laws, shot noise is given by Poisson statistics and the variance of fluctuations σ_e equals the mean electron number of accumulated electrons μ_e .
Other noise sources depend on the specific build of the detector, but due to the linear signal model they simply add up and can be grouped in two origins. Noise originating from sensor circuits and the amplifier can be characterized by a normal distributed noise σ_d which is independent on the signal. The analogue to digital conversion adds another uniform distributed noise source which is given as $1/12DN^2$.
Now, one can calculate the variance of the mean signal according to error propagation as

$$\sigma_y^2 = K^2\sigma_d^2 + \sigma_q^2 + K(\mu_y - \mu_{ydark}) \tag{4.1.4}$$

which is the central equation for characterizing a camera sensor.
Lastly one can have a look at the SNR, which basically describes the signal quality and should be maximized during the measurement. It is described as

$$SNR = \frac{\mu_y - \mu_{y,dark}}{\sigma_y} = \frac{\eta\mu_p}{\sqrt{\sigma_d^2 + \sigma_q^2/K^2 + \eta\mu_p}}. \tag{4.1.5}$$

In this thesis the detector is used in the high photon limit of the equation above

$$SNR \approx \sqrt{\eta\mu_p} \tag{4.1.6}$$

which can be applied if $\eta\mu_p \gg \sigma_d^2 + \sigma_q^2/K^2$. In this approximation the quantum efficiency is the only parameter which distinguish a real sensor from an ideal one. Following this argumentation a higher quantum efficiency of the detector has a direct impact on the image quality.

4.2 The dark current and offset images

The dark current of the instrument is briefly investigated by two different measurements. First, the dark current is determined by a measurement of the mean dark signal within a range of exposure times. Second, the dark current is investigated for different numbers of averaged images to investigate noise reduction.
To characterize the dark current a measurement of the dark current for 7 different exposure times in the range of $10\mu s$ up to $10s$ for a temperature of $0°C$ is done.

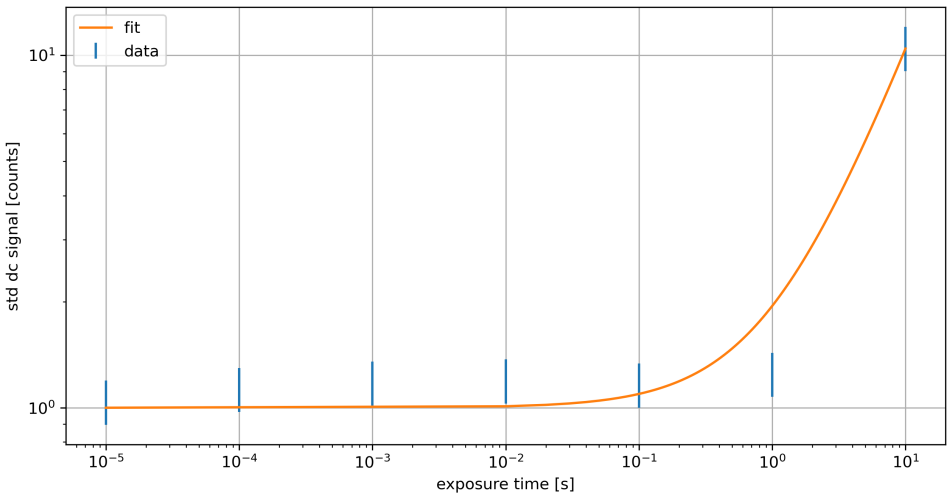

Figure 4.2.1: Plot of the standard deviation of the dark current signal against the exposure time in seconds. The blue curve shows the data and the orange curves a linear fit.

The result of this measurement is shown in Figure 4.2.1. For the investigation of the dark current an average over 50 images per exposure time is performed. Then, the standard deviation over an area of 1000×1000 pixel in the middle of the averaged dark current images is calculated and plotted against the exposure time of the measurement. The resulting curve is fitted with a linear function, resulting in a dark current signal of

$$\mu_{dark} = (0.95 \pm 0.02)\frac{counts}{s}. \tag{4.2.1}$$

To compare this value to the manufacturers declarations of $0.2e^-/s$ a conversion into e^-/s is done with the conversion factor of $0.8e^-/counts$ (AG (2021)) resulting in

$$\mu_{dark} \approx 0.75\frac{e^-}{s}. \tag{4.2.2}$$

The measured result differs strongly from the manufacturers declaration. A possible reason for this result is the chosen temperature of $0°C$. The detector is able to cool up to $-25°C$ and under the assumption of a typical dark current doubling temperature in the range of $7°C$ the measurement and the expectation come very close. For further experiments it is planned to operate the detector at a cooling point of $0°C$ for a stable dark current correction. The temperature has been chosen from a trade-off between maximum cooling and power consumption, taking into account the operation of the camera under field conditions.

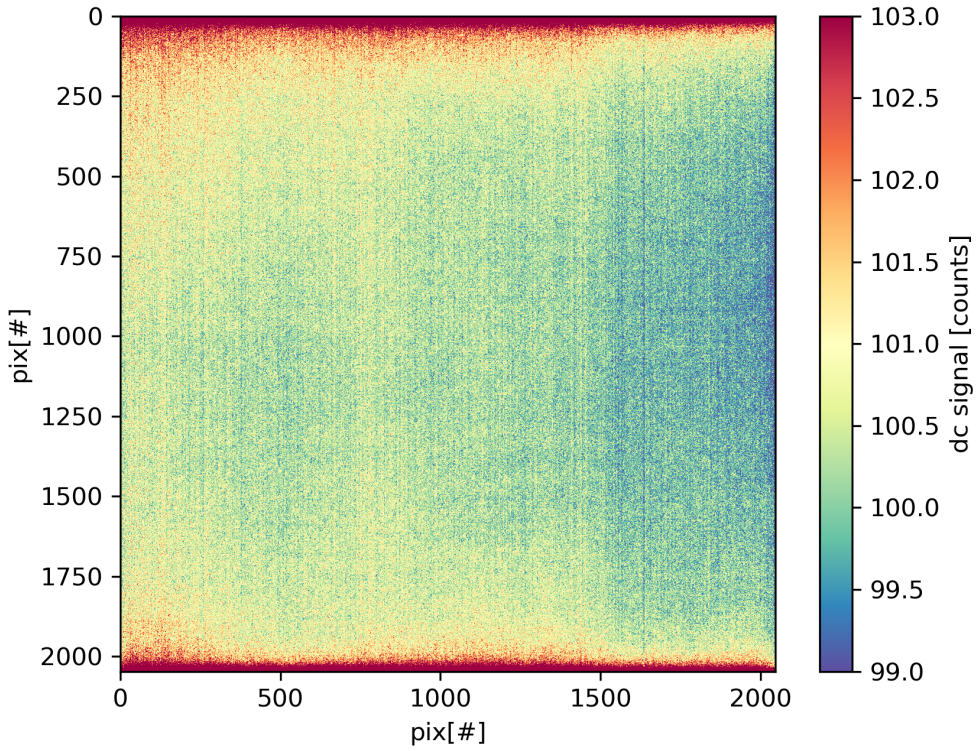

Figure 4.2.2: Mean dark current image averaged over 200 single images. The mean signal in counts is displayed through the colour code.

In Figure 4.2.2 an exemplary dark current image from a measurement series is shown. Plotted is a mean value over 200 dark current images with an exposure time of $0.3s$. The detector is cooled to a temperature of $0°C$. The exemplary image shows typical structures of a dark current image of a CMOS sensor as for example the vertical stripes which originate from the readout electronics, the high values at the upper and lower boundary which also originates from electronic effects. Additionally, some hot pixels are visible, which have much higher dark current signals compared to other pixels.
Next, the noise behaviour of the dark images is investigated.

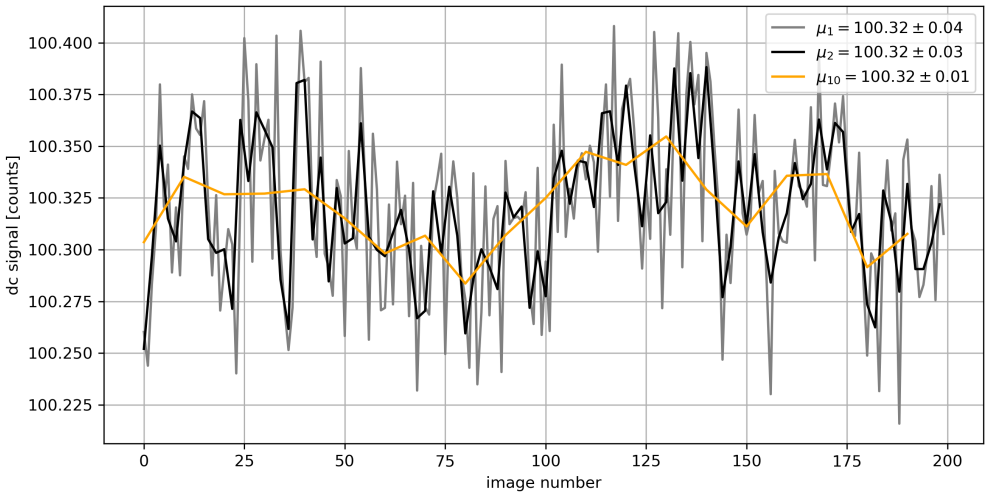

Figure 4.2.3: Plot of the mean dark current signal against the image number. The grey line shows the mean signal for each image, the black line for an average over two images and the orange line for an average over 10 images.

To investigate this properties a mean value of the dark signal of a dark current image series is plotted against the image number in Figure 4.2.3. Additionally the the mean value and the standard deviation for this series are calculated. To investigate the noise behaviour the single image series (grey line in Figure 4.2.3) is compared to mean values over 2 images (black line in Figure 4.2.2) and over 10 images (orange line in Figure 4.2.3). This yields the following results

$$\begin{aligned} \mu_1 &= 100.32 \pm 0.04 \\ \mu_2 &= 100.32 \pm 0.03 \\ \mu_{10} &= 100.32 \pm 0.01. \end{aligned} \tag{4.2.3}$$

If one looks at the scaling factor of the error, it turns out that it corresponds to the statistical expectation. For an average of 2 images the scaling factor equals to $\approx \sqrt{2}$ and for 10 images to $\approx \sqrt{10}$.

4.3 The pixel shift between on-band and off-band image

One of the most important corrections is the offset between the on and off-band image due to the different FPI angles. Following Snell‘s law light beams traversing a medium with a higher refractive index lead to a parallel displacement between

incoming and outgoing beam. This happens twice in the FPI due to the two glass plates. For the evaluation of 2 dimensional differential optical densities it is essential to align both images correctly. If the alignment of the images is not as exact as possible, then an evaluation of the images is only possible with a large error. To correct for this affect an affine image transformation is used. To calculate the transformation matrix a strong intensity gradient in the image is beneficial. This could be achieved for example by moving a mountain ridge, a gas cell edge or a building into the FOV and use this as a natural intensity boundary. The correction between the two images lies in the range of 40 pixels in the vertical direction. A horizontal shift is not expected, since the optical setup produce parallel light beams and the FPi is tilted only on the horizontal axis. For the calculation of the pixel shift the Enhanced Correlation Coefficient (ECC) Maximization is used. This algorithm is based on the work of **?** and is used from the python open-cv library. In principle the algorithm is able to estimate image transformation up to homographic level but here only two parameters for a shift in x- and y-direction are estimated which results in a simple image translation. The result of the algorithm is a $2x3$ matrix which has a unity block in the first four entries and the x and y shift in the remaining entries. In principle only a shift in the vertical direction (y-direction) is expected, but if the instrument does not stay level an horizontal shift (x-direction) is introduced as well. A secondary feature of the pixel shift is the ability to check the stepper motor accuracy with it. For this measurement the pixel shift for every image pair is plotted against the image number.

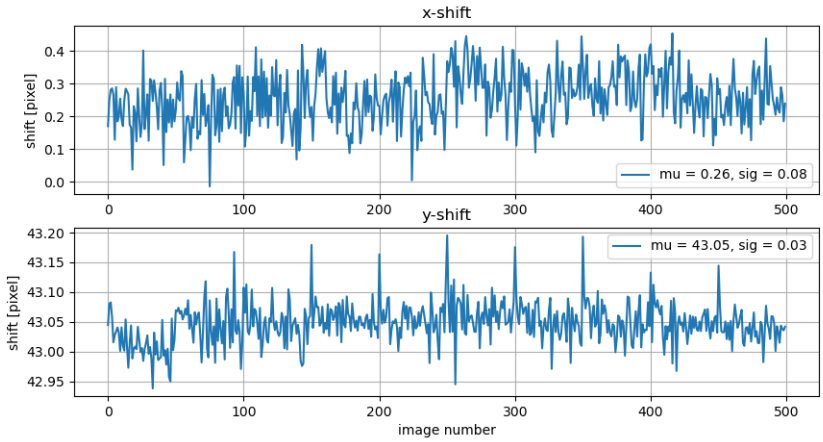

Figure 4.3.1: Upper panel shows the shift in x-direction and the lower panel shows shift in y-direction for a single data set between off-band and on-band images.

In Figure 4.3.1 a comparison of an exemplary dataset to check the motor accuracy is shown. As a first expectation the pixel shift should stay mainly constant for the whole dataset. A slight noise of the stepper motor is expected as well, but in this measurement the standard deviation of the pixel shift is much smaller than 1 pixel.

From this measurement one obtains that the motor accuracy is rather constant over a measurement and does not introduce additional problems.

4.4 The flat field image investigation

The flat field images play an important role for the evaluation. They should remove instrumental effects, reduce noise and correct for the background. In this chapter effects originating from different flat fields are discussed. The flat field images from different daytimes, which results in different relative solar azimuth angles (SAA), with different inclinations, which results in different intensity profiles of the sky and with different acquisition modes, are compared. For this purpose the flat field images are evaluated against each other by calculating the differential optical density between an off-band and an on-band flat image. This method is used to exclude disturbances from plume movements or other trace gas effects. Ideally, one would expect that the measurement does not depend on the chosen flat field, at least in a short tim period between measurement image and flat field image acquisition. Problems arise, when horizontal or vertical gradients are introduced, because the differential evaluation process has the implicit assumption that the background stays constant for the on-band and off-band position.
First, the effect of the acquisition technique is investigated. Here two methods are possible. The alternating method, where on and off-band images are recorded alternately and the non-alternating mode, where first all on-band images and afterwards the off-band images are recorded.

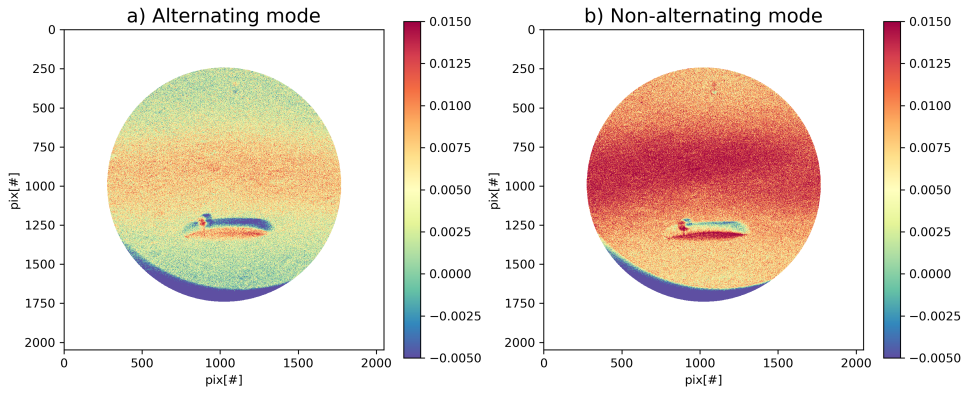

Figure 4.4.1: Comparison of a flat field evaluation for the alternating image acquisition mode (left panel) and the non-alternating mode (right panel). The colour scale shows the AA.

The evaluated images shown in Figure 4.4.1 are recorded with an exposure time of $0.3s$ at a time of 07:27 to 07:30 UTC on the 9th of October 2020. The elevation angle of 31° and the viewing direction of $20°N$ are held constant for both measurements. Before one takes a look on the result of this measurement, the general

structure of an IFPICS image is shortly introduced based on Figure 4.4.1. IFPICS images have a round illuminated cut out because of the FPI clear aperture. This cut out is tunable and the tuning process is called optical binning introduced in the instrument section 3.3. The edge area is ignored for further evaluation. In the middle part of the image a bright horizontal structure is visible. This is a remnant of a reflective point originating from the instrument optics. The reflective point decreases for higher tilt angles of the FPI. Due to that it is only visible in the off-band position, but through the differential evaluation it results in a very strong feature. For the measurements it is important to place this structure in an unimportant part of the image, for example in the crater flank of a volcano.
Now, the comparison of the two acquisition mods displayed in Figure 4.4.1 is discussed. Both images show a vertical gradient with a maximum in the middle of the image, but the gradient in the non-alternating mode (see Figure 4.4.1 b)) shows a larger vertical gradient of roughly 0.01 in the AA which is twice as large as in the comparison picture for the alternating-mode image (see Figure 4.4.1 a)). Due to that, the alternating image acquisition is strongly recommended and has been used for all the measurements presented in this work.
Next, one takes a look at the effect of different solar azimuth angles and different elevation angles of the camera. This is from particular importance because the measurement geometry only allows for flat field images above the plume with a high elevation angle or beside the plume in a sky area with a different relative solar azimuth angle. The next measurement presented here has the same measurement parameters as above except for the elevation angles and the relative SAA.

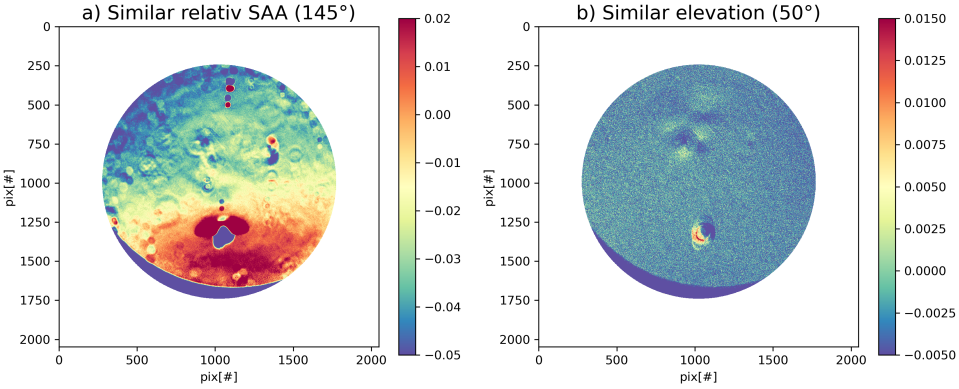

Figure 4.4.2: a) Effect of different elevation angles($30° - 50°$) for the same SAA on the evaluation of flat field images b) Effect of different relative SAA ($145° - 156°$) at the same elevation angle of $50°$ on evaluated flat field images.

The result of a measurement with a strong difference in the elevation angle of $20°$ can be found in the left panel Figure 4.4.2. The comparison shows a strong vertical gradient in the image of up to 0.07 in the AA signal. This effect has a strong influence

on the image compared to the acquisition mode measurement in Figure 4.4.1. In conclusion one should reduce the evaluation angle between measurement and flat field as much as possible for example by taking flat fields on the side of the plume instead of above the plume. The effect of a change in the relative SAA is shown in the right panel of Figure 4.4.2. This flat field images were recorded at a similar elevation angle of 50° but with a time difference of 30 min corresponding to change in relative SAA of 11° and one can clearly identify that the strong vertical gradient from the previous examination is nearly vanished and only a slight horizontal gradient remains which possibly originates from the change in relative SAA. This result supports the finding from the previous evaluation that flat field images should be recorded with the same elevation angle of the camera.

4.5 The optical flow correction

The imaging technique introduced in this work relies on one detector and a rotatable FPI. Because of the chosen setup, images must be acquired in an alternating manner. Due to this setup it is very difficult to evaluate fast moving intensity gradients in the image, as for example present in volcanic plumes at high wind speeds. There the time delay between on-band and off-band image is large enough to introduce strong false signals, through the differential evaluation. The resulting false signals can be identified as structures with a very strong gradient in the evaluated images and a highly positive signal in the direct neighbourhood of a strong negative signal. Correcting for this effect is essential for evaluation and to account for this effects an optical flow algorithm is used.
Generally optical flow describes the motion pattern of objects between two consecutive captured images. Imagine an object with intensity $I(x, y, t)$ moves by dx and dy after a time dt. The new intensity is given as $I(x + dx, y + dy, t + dt)$ and under the assumption of constant pixel intensities between these two frames one gets

$$I(x, y, t) = I(x + dx, y + dy, t + dt). \tag{4.5.1}$$

Evaluating the right hand side of this equation by Taylor approximation leads to

$$\frac{dI}{dx}\delta x + \frac{dI}{dy}\delta y + \frac{dI}{dt}\delta t = 0. \tag{4.5.2}$$

Dividing the result by δt yields the Optical Flow Equation

$$\frac{dI}{dx}u + \frac{dI}{dy}v + \frac{dI}{dt} = 0 \tag{4.5.3}$$

with the velocities u, v in x and y-direction.The algorithm used in this thesis is based on the work of Farnebaeck (2000) and is available through the open-cv python

library. It is a dense optical flow algorithm that takes intensity changes in every pixel of the image into account. The algorithm enables one to calculate the magnitude and direction of optical flow from an array of flow vectors between two consecutive images taken at times t_i and t_{i+1}. With the resulting optical flow field one can determine the image in between this two images at a time $t_{i+\frac{1}{2}}$. In this work the optical flow correction is used for the off-band images.

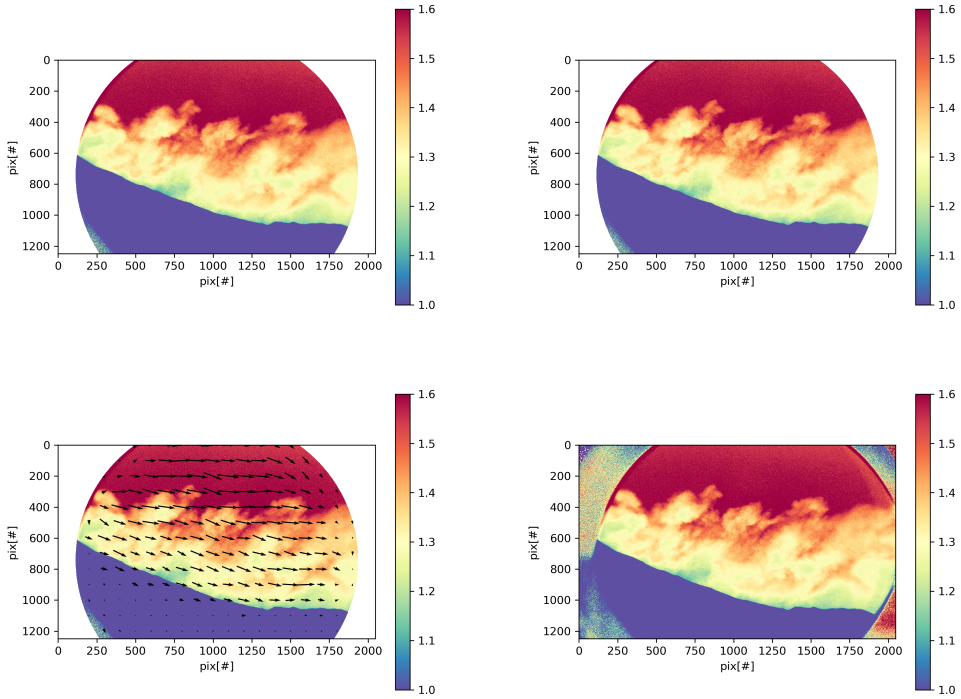

Figure 4.5.1: Exemplary image series of the optical flow calculation and correction. The first row show two off band images recorded at times t_i (left) and t_{i+1} (right). Between this two images an optical flow field (black arrows) is calculated and plotted above the plume area in the left image in the second row. The right image in the second row shows the off-band image calculated with optical flow at a time of $t_{i+\frac{1}{2}}$.

In Figure 4.5.1 the working principle of the optical flow field calculation for a measurement at Mt Etna in October 2020 is illustrated. One has a 90° viewing angle on the plume of the south east crater. In the lower part of the images the crater flank is visible. Above the crater flank first the plume is visible and afterwards the sky background. The first row displays both off-band images at times t_i and t_{i+1}. The lower row shows the calculated optical flow field (left panel) and the calculated off-band image at a time $t_{i+\frac{1}{2}}$ using this flow field (right panel). The magnitude of the velocity field is described by the length of an arrow. The algorithm does not run over the complete image, only a square area covering the plume has been used.

For convergence the algorithm needs strong intensity gradients and due to that only the important part of the image is cut out to reduce side effects. It is clearly visible that the strongest movement happens within the plume. Sky and crater flank area do not contribute much in the optical flow field. The resulting image of the optical flow calculation looks very similar to initial images. A further application of this calculation is to infer an estimation of the wind speed through analysis of the flow field. This is from particular importance for trace gas flux calculations.

4.6 The high pass filter correction

Because of the image shift in y-direction due to the two FPI positions the flat field images only correct for instrumental effects in the image plane. But dust sitting on the optics behind the FPI does not experience the parallel offset due to the FPI glass plates. If one corrects for the pixel shift theses structures result in strong false signals in the evaluated images. To correct for this effects a high pass filter correction is used. Before using this correction one has to check if the structures seen on the evaluated images are really constant which is done by looking at an average over a complete AA image series. The averaging time is typically in the order of 10 min. The first step of building a high pass filter correction image is to produce an average over a complete AA image series. This average AA image is than filtered by a Gaussian low pass filter. The result is an image which contains only low frequency structures. Subtracting this low pass filtered image from the average AA image leads to an image which contains only the high frequency features. This high pass filter correction image is used in the evaluation process to correct for high frequency structures by a simply subtracting it from the evaluated measurement images.

In Figure 4.6.1 a detailed image series of high pass correction calculation is shown. The left panel shows the average over the complete AA image series which is corrected by a Gaussian low pass filter in the middle panel. The Gaussian filter has a standard deviation of 100 pixels. It is visible that the low pass correction leaves only the low-frequency structures. Subtractin this from the average AA image leads to the high pass correction image which than contains only high frequency structures as seen in Figure 4.6.1 (right panel). It is important to cut out the central part of the image, for example the sky and the plume area, because the Gaussian low pass filter reacts very sensible to large gradients, for example at the image edges.

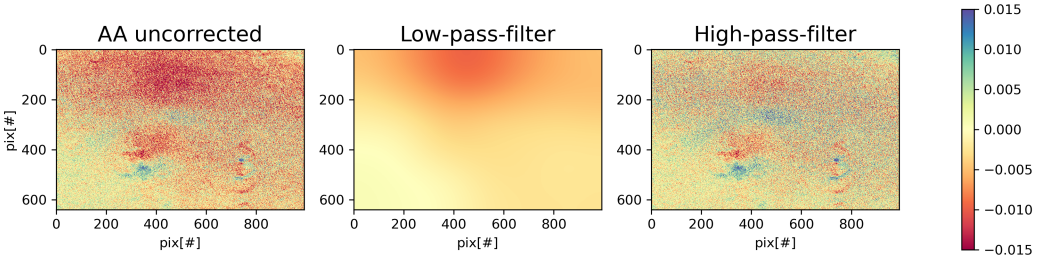

Figure 4.6.1: Exemplary calculation of a high pass filter correction image. The left panel (AA uncorrected) shows an average over a total AA image series. The middle panel (Low-pass-filter) shows a low pass correction of the left image with a Gaussian low pass filter with a standard deviation of 100 pixels. The right panel (High-pass-filter) shows the subtraction of the two other images and is the high pass filter correction image used in the evaluation.

5 Imaging measurements and calibration modelling

5.1 The IFPICS model results for BrO and HCHO

In this section the results of the forward instrument model (see section 2.4.2) are discussed. The AA is investigated as a function of the angle of incidence α on the FPI. This simulation yields the positions of maximum correlation between the FPI transmission and the absorption structure of the target trace gas. Furthermore a calibration curve is calculated giving the expected AA signal for a range of column densities. Additionally, a short description of the similarities between HCHO and BrO at a wavelength of $(340 \pm 5)nm$ is given.

Parameter	Value	Description
O_3 VCD [DU]	335	O_3 vertical column density
$\Delta\lambda$ [nm]	320 - 359	wavelength range of simulation
R	0.70	FPI reflectivity
F	8.54	FPI finesse
d [μm]	12.330	FPI plate distance
n	1.00028	FPI refractive index (air)
a [mm]	1.1	aperture opening
f [mm]	47	focal length of lens sytem 1

Table 5.1: Model parameters as described in section 2.4.2

The model parameters are shown in Table 5.1. All parameters are chosen according to the FPI used for the measurements and the optical components used in the instrument setup. The radiances are taken from a solar atlas spectrum and are scaled according to a Rayleigh scattering atmosphere and including stratospheric O_3 absorption (see section 2.4.2). First modelling step is to calculate the integrated detected radiances $I_{FPI}(\alpha)$ containing the trace gas absorption and $I_{0,FPI}(\alpha)$ without trace gas as a function of the incidence angle α in an angle range between $[0°, 12°]$. The absorption cross sections for HCHO σ_{HCHO} and BrO σ_{BrO} are obtained from Chance and Orphal (2011) and Fleischmann et al. (2004), respectively. The variation of the incidence angle introduces mainly a shift of the FPI transmission spectrum. The progression of tau_{FPI} represents the shift of the FPI transmission across the trace gas absorption spectrum and allows finding the optimum FPI tilt angles for an on-band and off-band measurement. The representation of this progression is often referred to in the following as an interferogram. When the optimal tilt angles are

found, a calibration curve is calculated. The incidence angles are kept constant at $\alpha_{on-band}$ and $\alpha_{off-band}$ and the column density S of the target trace gas is varied, which gives the calibration curve from $AA_{FPI} = k \cdot S$. The instrument sensitivity k is determined by a linear fit of the calibration curve.

5.1.1 The model results for HCHO

In this section the model results for HCHO are shown. First, the progression of τ_{FPI} over the angle of incidence α is simulated. For that, a trace gas column density of $S_{HCHO} = 5 \times 10^{16} molec/cm^2$ for HCHO is chosen, which easily can be also achieved in the gas cells. In Figure 5.1.1 the calculated optical densities τ_{FPI} are plotted against the angle range.

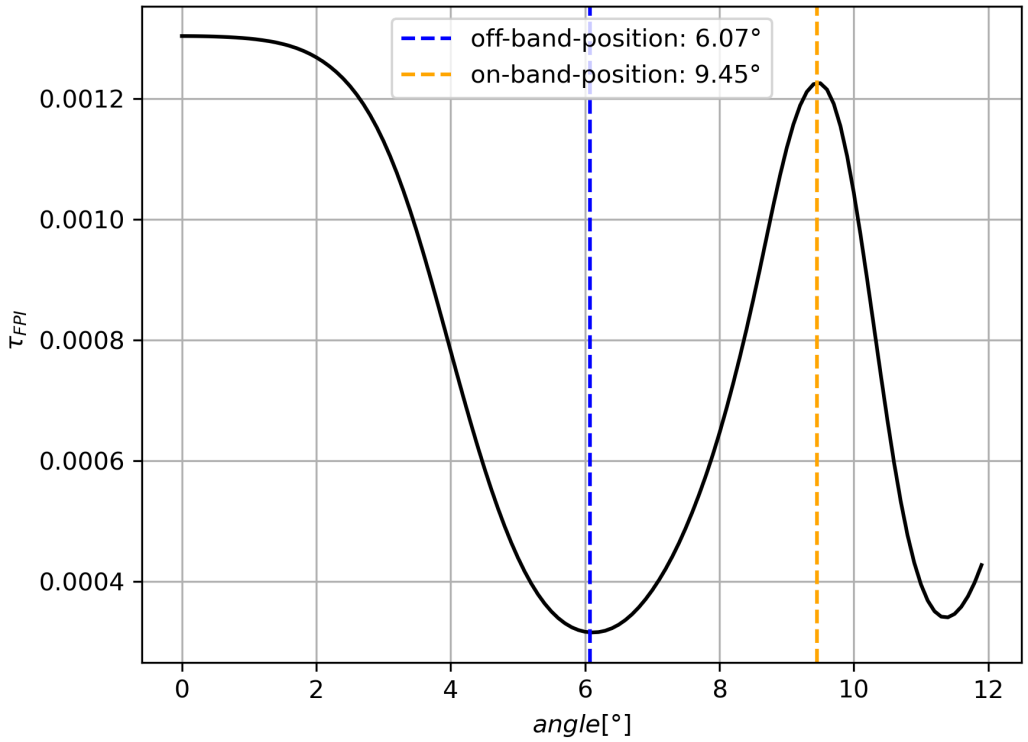

Figure 5.1.1: Modelled interferogram for HCHO. The marked positions show the measurement positions, e.g. the FPI tilt angles at the on-band (orange) and the off-band (blue) position.

The dashed lines show the chosen on-band and off-band positions yielding maximum correlation with the narrowband absorption structures of HCHO. The actual maximum at 0° cannot be used, because of the reflective point of the optical setup. The effect through this reflection decreases towards higher tilt angles of the FPI.

Due to that, for the measurement the following angles are chosen

$$\begin{aligned} \alpha_{on-band} &= 9.45° \\ \alpha_{off-band} &= 6.07°. \end{aligned} \tag{5.1.1}$$

The difference between the optical density at on-band position $\tau_{on,band}$ and off-band position $\tau_{off,band}$ in Figure 5.1.1 yields an AA signal of approximately 1×10^{-3} for the chosen HCHO column density. The corresponding transmissions for the two FPI positions are shown in Figure 5.1.2.

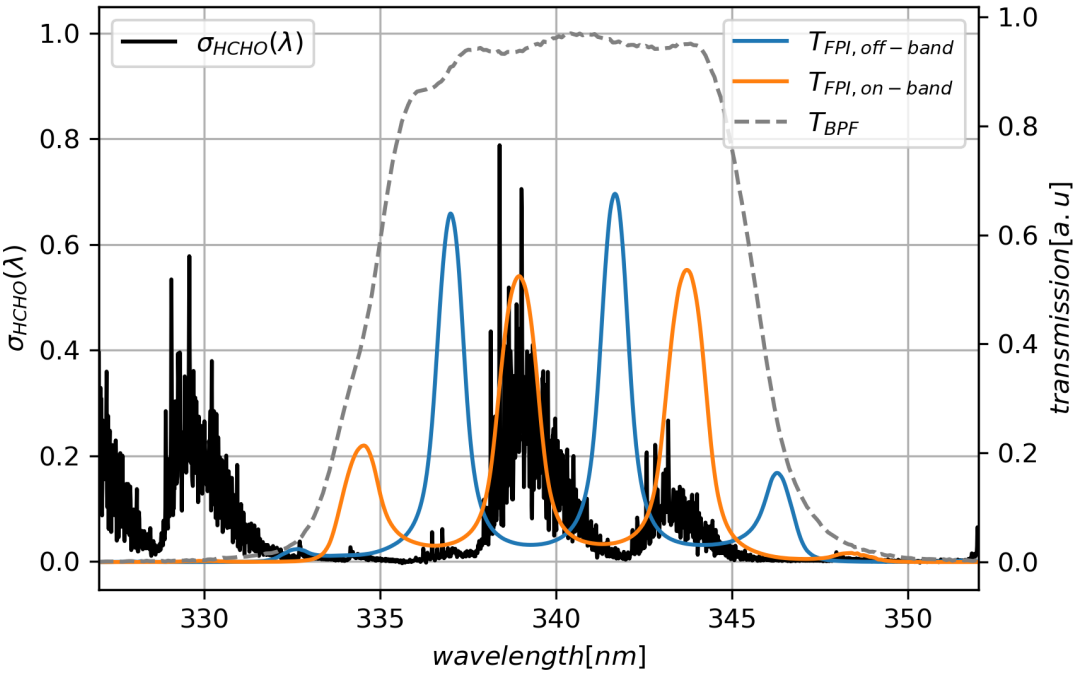

Figure 5.1.2: Transmissions of the two FPI positions (T_{FPI,on_band} (orange) and T_{FPI,off_band} (blue)) and absorption cross section of HCHO σ_{HCHO} (black) over the wavelength. The band-pass transmission T_{BPF} is displayed with the grey dotted line.

By now using the calculated angles $\alpha_{on,band}$ and $\alpha_{off,band}$ allows calculation of the calibration function. The incidence angles are kept constant at $\alpha_{on-band}$ and $\alpha_{off-band}$ and the column density S_{HCHO} is varied between $1 \times 10^{15} molec/cm^2$ and $3 \times 10^{17} molec/cm^2$.

The resulting calibration curve for HCHO is displayed in Figure 5.1.3. Fitting a

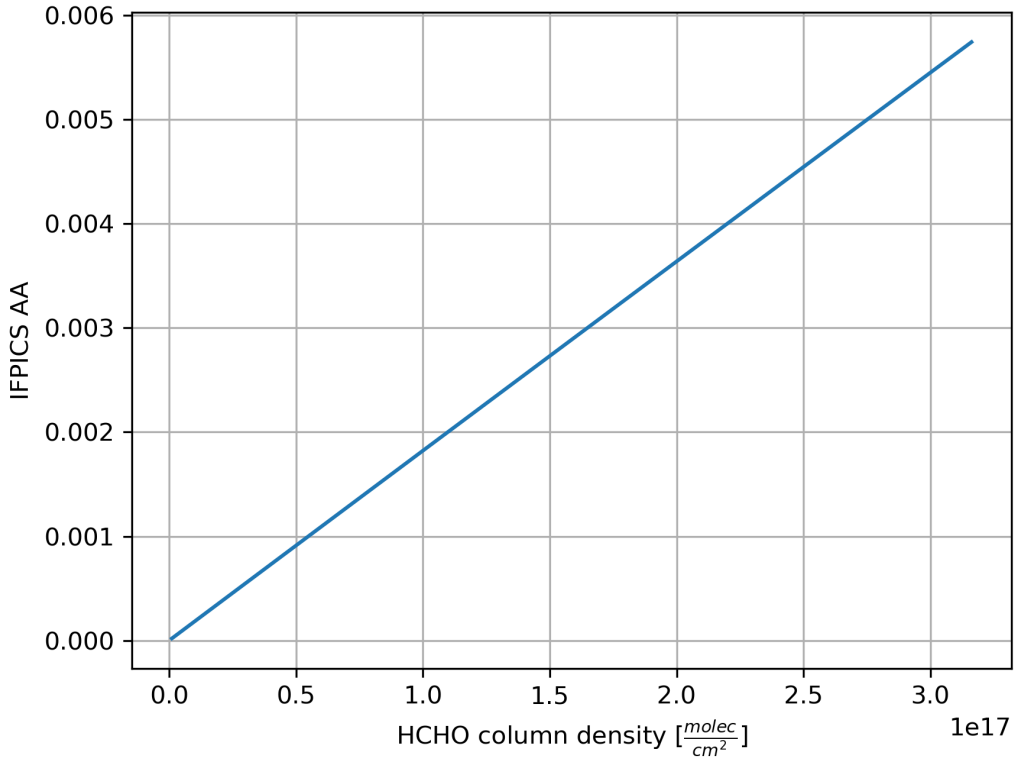

Figure 5.1.3: Simulated calibration curve for HCHO, which shows the expected IF-PICS AA signal for a given trace gas column density.

linear function to the calibration curve leads to the following conversion factors

$$\begin{aligned} AA_{HCHO} &= (1.8178 \pm 0.0001) \times 10^{-20} \frac{cm^2}{molec} \cdot S_{HCHO} \\ S_{HCHO} &= (5.5012 \pm 0.0003) \times 10^{19} \frac{molec}{cm^2} \cdot AA_{HCHO} \end{aligned} \tag{5.1.2}$$

with a correlation coefficient of $R = 0.99$. Under the assumption of a AA detection limit of 1×10^{-3} the simulated conversion factor results in a minimum measurable column density of $5.49 \times 10^{16} molec/cm^2$. Compared to the non-divergent beam model from Fuchs (2019) sensitivity decreases because the transmission intensity and sharpness of the FPI transmission maxima is reduced which leads to a smaller difference between on-band and off-band position. To quantify this loss the ratio between the conversion factors $\delta k_{HCHO} = 0.91$ is calculated, which results in 9% sensitivity loss. In the simulated column density range no saturation effects occur. The linear approximation is valid under the assumption of $\sigma \cdot S \ll 1$. Stronger trace gas optical densities would lead to flattening of the calibration curve and the simple linear conversion is not applicable any more.

5.1.2 The model results for BrO

For the BrO modelling the steps are equal to the HCHO model section 5.1.1. For BrO a column density of $S_{BrO} = 2 \times 10^{14} molec/cm^2$ was assumed, which is measured in the plumes of several volcanoes Bobrowski and Giuffrida (2012). Following the section on HCHO modelling, the optical density progression for BrO for the given FPI is calculated and shown in Figure 5.1.4.

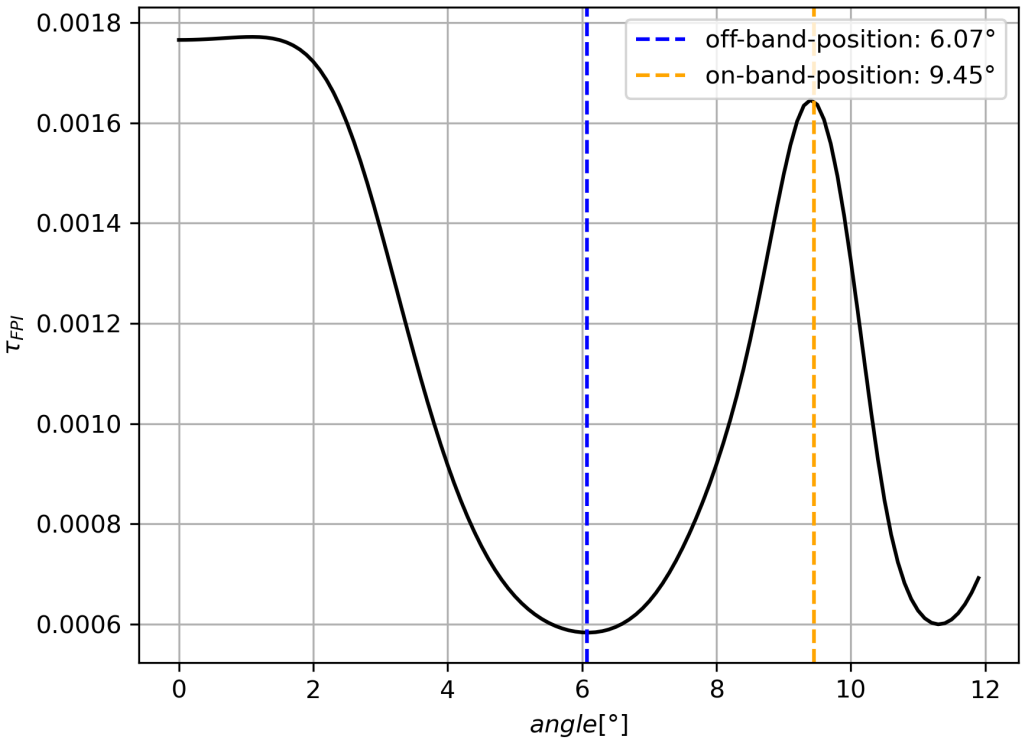

Figure 5.1.4: Modelled interferogram for BrO. The marked positions show the measurement positions, e.g. the FPI tilt angles at the on-band (orange) and the off-band (blue) position.

The angles for maximum and minimum correlation coincide with the simulated angles of HCHO. A discussion of the similarities between BrO and HCHO is given in section 5.1.3. To underline this result the FPI transmissions for the BrO model result are displayed in Figure 5.1.5.

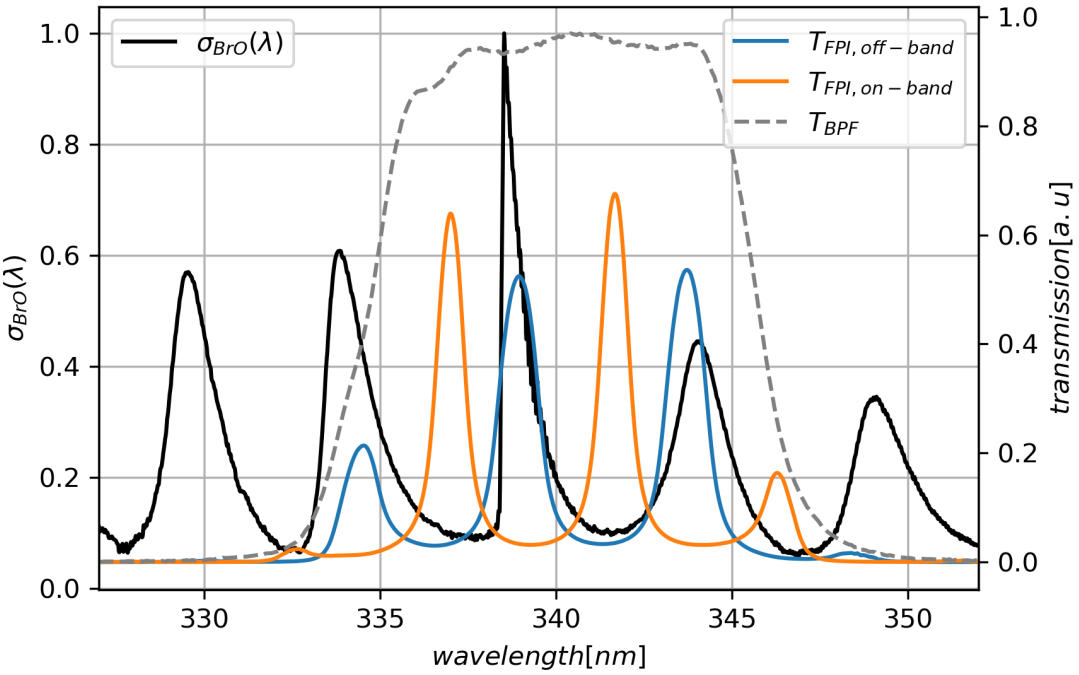

Figure 5.1.5: Transmission intensities of the two FPI positions (I_{FPI,on_band} (orange) and I_{FPI,off_band} (blue)) over the absorption cross section of BrO σ_{BrO} (black). The band-pass transmission is displayed with the grey dotted line.

The calibration function for a BrO in a column density range of $1 \times 10^{13} molec/cm^2$ and $6 \times 10^{14} molec/cm^2$ is displayed in Figure 5.1.6.

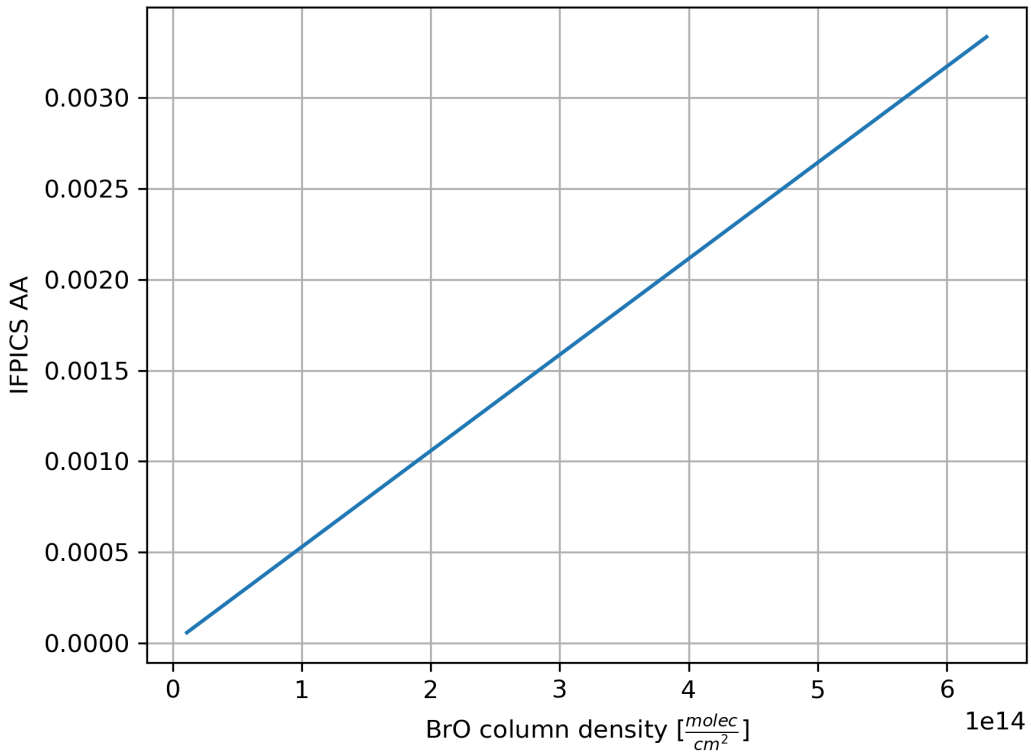

Figure 5.1.6: Simulated calibration curve for BrO

Analogously to the HCHO calibration linear fitting leads to the linear conversion factors as

$$\begin{aligned} AA_{BrO} &= (5.288 \pm 0.002) \times 10^{-18} \frac{cm^2}{molec} \cdot S_{BrO} \\ S_{BrO} &= (1.891 \pm 0.001) \times 10^{17} \frac{molec}{cm^2} \cdot AA_{BrO} \end{aligned} \tag{5.1.3}$$

with a correlation coefficient of $R = 0.99$. Under the assumption of the same AA detection limit of 1×10^{-3} as before a column density of $1.89 \times 10^{14} molec/cm^2$ is expected. To give an estimation on the reduced sensitivity compared to Fuchs (2019) the conversion factor ratio is calculated again as $\delta k_{BrO} = 0.85$. Here the loss is larger than for the HCHO simulation at 15%. Summing up the simulation chapter one can conclude that detection of typical volcanic BrO column densities requires an AA detection limit in the magnitude of 1×10^{-3} or even lower.

5.1.3 The similarities between HCHO and BrO

In this section the benefits and downsides of the strong correlation between the absorption cross sections of BrO and HCHO are discussed. In Figure 5.1.7 a com-

parison between the cross sections of both gases is given.

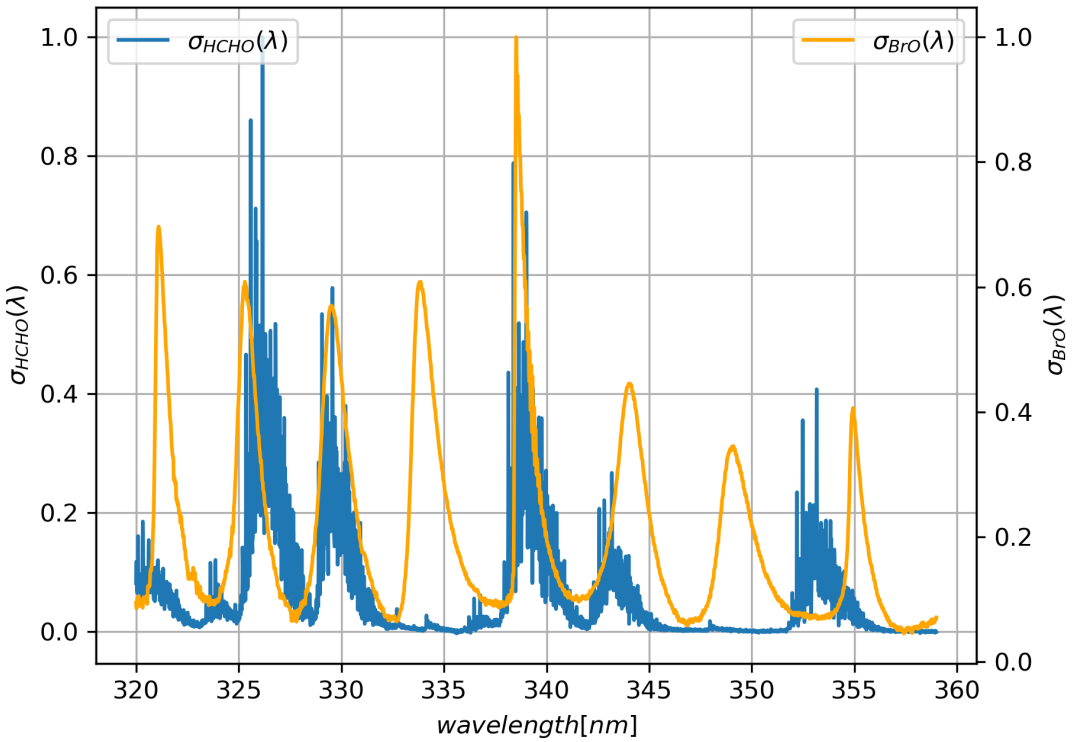

Figure 5.1.7: Comparison of the absorption cross sections of HCHO (blue) and BrO (orange). Both cross sections are normalized.

From Figure 5.1.7 one can obtain that both gases show a strong correlation in the spectral range around $340nm$. As shown in the previous section (5.1.1, 5.1.2) instrument parameters are about the same for both gases.
This means that HCHO and BrO are not distinguishable within a measurement, once they are both present in significant amounts. Due to that, pre knowledge on the measurement is necessary. Detection of BrO for example, can only take place under the assumption that there is no measurable concentration of HCHO in the plume. In volcanic plumes in an atmospheric background with low pollution (e.g. at large altitudes) very low levels of HCHO are expected. In this case, the instrument signal can be entirely related to BrO.
In cases, where both gases are present the issue could be resolved by an additional (i.e. a third) FPI tuning setting, which captures the differences of the BrO and HCHO absorption spectrum. The sensitivity of the measurement of the individual species will then be strongly reduced. This is up to date only a hypothetical solution, because the current detection limit of the instrument is not sufficient to allow for a detection with non optimal FPI tilt positions. But the similarity of the two gases

has not only disadvantages. BrO exhibits a self reaction and in combination with the limited light path of the experiments it is very difficult to handle it in the laboratory or in form of gas cells. Due to that issue imaging of BrO is only possible at strong natural emitters as for example at volcanoes, which is unpractical for proof of concept or test measurements. HCHO on the other hand can be treated in the laboratory in form of gas cell with para-formaldehyde, which can be heated by a heat gun to produce gaseous HCHO. Here the similarieties between both gases are employed and HCHO measurements are used as a proxy for BrO simply by inferring the ratio of both absorption cross sections.

5.2 HCHO imaging measurements

In this section imaging of HCHO gas cells is introduced. One uses quartz glass cuvettes filled with para-formaldehyde which is a white solid powder and can be evaporated with a heat gun producing gaseous HCHO. For imaging measurements different light sources are available. In general, scattered skylight is preferred in order to reproduce field conditions but integrating spheres or LED's are also suitable. As shown through model calculations the instrument setup will be the same for BrO and HCHO and due to that one can give a proof of concept of the measurement technique for BrO by measuring HCHO and convert this with the ratio of the cross sections into a theoretical BrO detection. From this approach a theoretical detection limit of BrO is calculated.

5.2.1 Gas cell angle scans

A first measurement to validate if the modelled angles corresponding to the on and off-band position coincide with the actual measured angles. This is done by recording an interferogram with HCHO gas cells. An imaging measurement of a gas cell is performed and the FPI is tuned over a distinct angle range between 4.2° and 11.2° in 0.2° steps. The gas cell is positioned in front of the camera and scattered skylight is used as a light source. To produce gaseous HCHO in the gas cell it is heated with a heat gun. Based on this procedure, it is to be expected that a strong HCHO signal is present at the beginning of the measurement, which decreases over time as the HCHO condenses back to para formaldehyde. Images are evaluated according to the procedure introduced in section 4. The mean value of the AA inside a squared area of the gas cell is plotted against the FPI tilt angle. In this measurement absolute values are not of interest (they will vary with the HCHO amount in the cell, which is temperature dependent) only the position of the minimum and maximum in the interferogram is important.

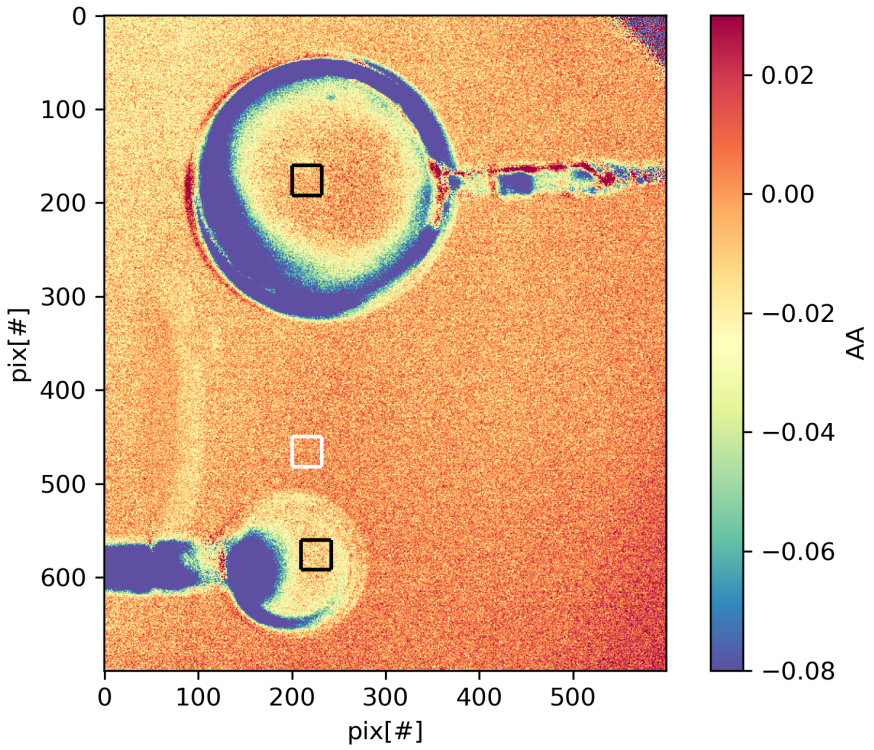

Figure 5.2.1: Exemplary logarithmic intensity image of a small and a large HCHO gas cell. The black boxes mark the averaging area inside the gas cells and the white box the background correction.

In Figure 5.2.1 an exemplary image of the angle scan time series is shown. The measurement was performed on the 18th of September 2020 at a time of 08:33 UTC. The measurement consists of 8 heated cell angle scans, two times 10 reference scans, which are images of the unheated gas cells and have been taken before and after the heated cell scans, and a dark current image series before the measurement. For the evaluation a mean value over the reference scans and the dark current scans is formed. All images were acquired with an exposure time of $1s$, which yields an detector saturation of approximately 5% and an output in the range of $1200 - 1300$ counts. Spatial binning of 2×2 pixels has been applied to all images resulting in a resolution of 1024×1024 pixel. The inner part is cut out for better visibility resulting in a frame size of 700×600 pixel.

The result of the measurement is displayed in Figure 5.2.2 including the model expectation for the on-band and off-band positions. The upper panel shows the results for the large gas cell and the lower panel for the small one. The averages over the gas cell area (black boxes in Figure 5.2.2) in the spatial dimension are effectively a mean over 64×64 pixel. The interferogram is normalized by subtracting its mean value. First, the interferograms show the expected structures with a minimum

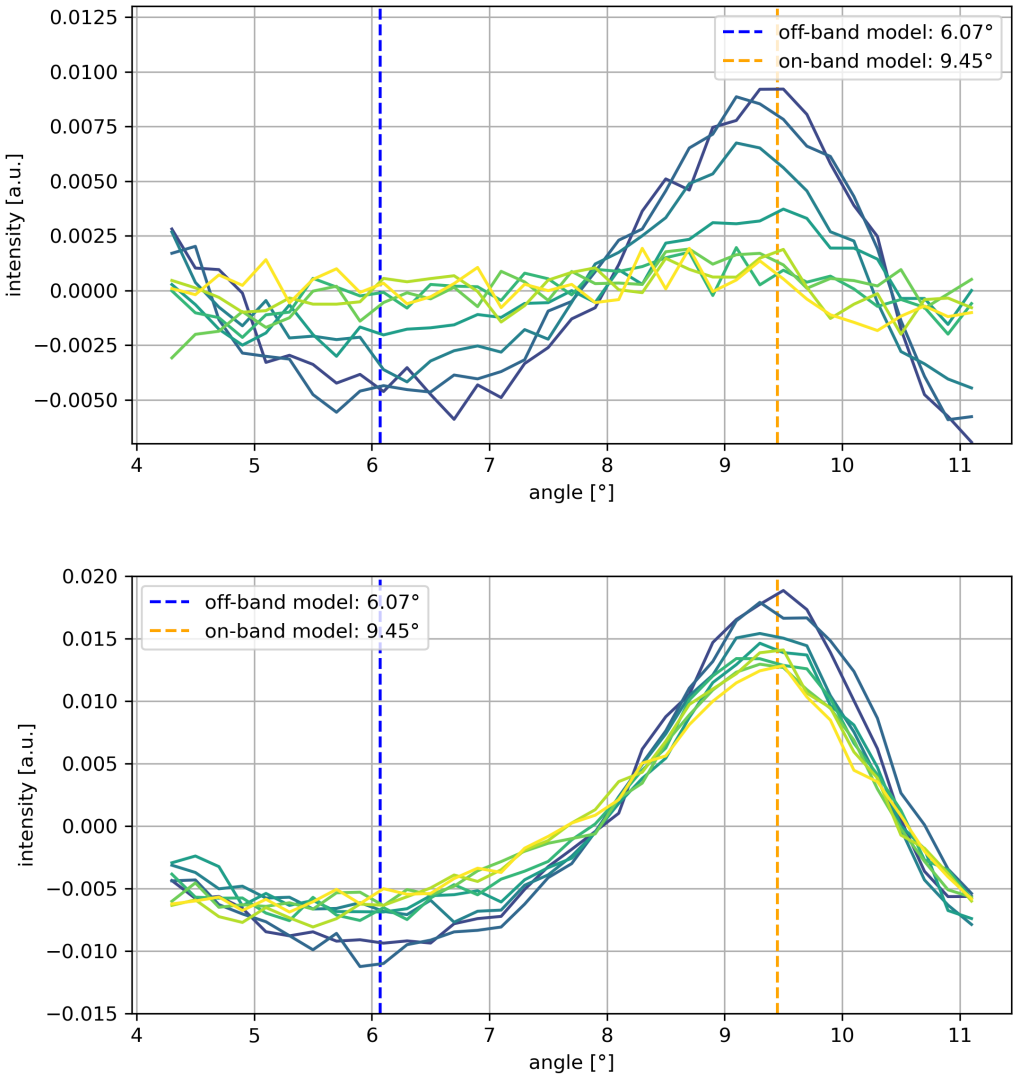

Figure 5.2.2: Interferogram measurement of a HCHO gas cells. The mean AA over the gas cell area is plotted against the tilt angle of the FPI. The modelled on-band (orange) and off-band (blue) angles are shown for comparison. The scan time is colour coded from blue to yellow. The upper panel shows the large gas cell and the lower panel the small one.

around 6° and a maximum around 9.5°. Following this observation, one can conclude that the actual measured interferograms nicely reproduce the expected angles for maximum correlation (on-band and off-band position) of the absorption structures of HCHO and the transmission of the FPI. Based on these measurements, the following angles

$$\begin{aligned} \alpha_{on-band} &= 9.45° \\ \alpha_{off-band} &= 6.07°. \end{aligned} \tag{5.2.1}$$

are used for further measurements. The measurement validates the model and should be performed before field campaigns or long journeys in order to check the instrument.

5.2.2 The alternating measurement

Next, alternating measurements are performed. During this measurement the FPI alternates between the on-band (9.45°) and off-band (6.07°) position calculated by the model (see section 5.1) and validated by the scan measurement (see sction 5.2.1). The measurement shown in Figure 5.2.3 was recorded on 19th September 2020 starting at 08:03 UTC with an exposure time of $1s$ per image. It consists of 400 measurement images, 80 flat field images, taken from the clear sky before the actual gas cell measurement, and 40 dark current images. Evaluation of the AA is done according to the data evaluation section. To reduce noise all images are binned (8×8 pixel) resulting in a resolution of 256×256 pixels.
The general measurement procedure is to start the measurement software and afterwards gas cells are heated starting with the large cell. Because of the time delay due to initialization of the stepper motor the large cell is heated at the begin of the measurement and only the heating process of the small cell is covered. Due to that procedure it is expected to observe a high AA signal at the beginning of the measurement inside the large cell. For the small cell an increasing value of the AA signal is expected which decreases after the heating process as well.

In Figure 5.2.3 several images from the AA time series are shown. The shown images correspond to the following time steps (1 min, 2 min, 7 min, 15 min) after measurement begin seen from left to right. As mentioned above the large gas cell shows a clear decrease of the AA signal over time. For the small gas cell the heating effect between image number 10 and 20 is clearly visible by a strong increase in the AA signal. From this one can see, that the small cell is much more stable over time and the decrease in AA is much smaller on the minute timescale shown here. To give a more quantitative description of the measurement the mean AA over the gas cells are calculated and plotted against the time.

The mean AA is displayed in Figure 5.2.4. The expected course of the signal from the series of images is also represented here. To have a more quantitative look at the time series one can observe a really strong AA signal in the small cell of roughly

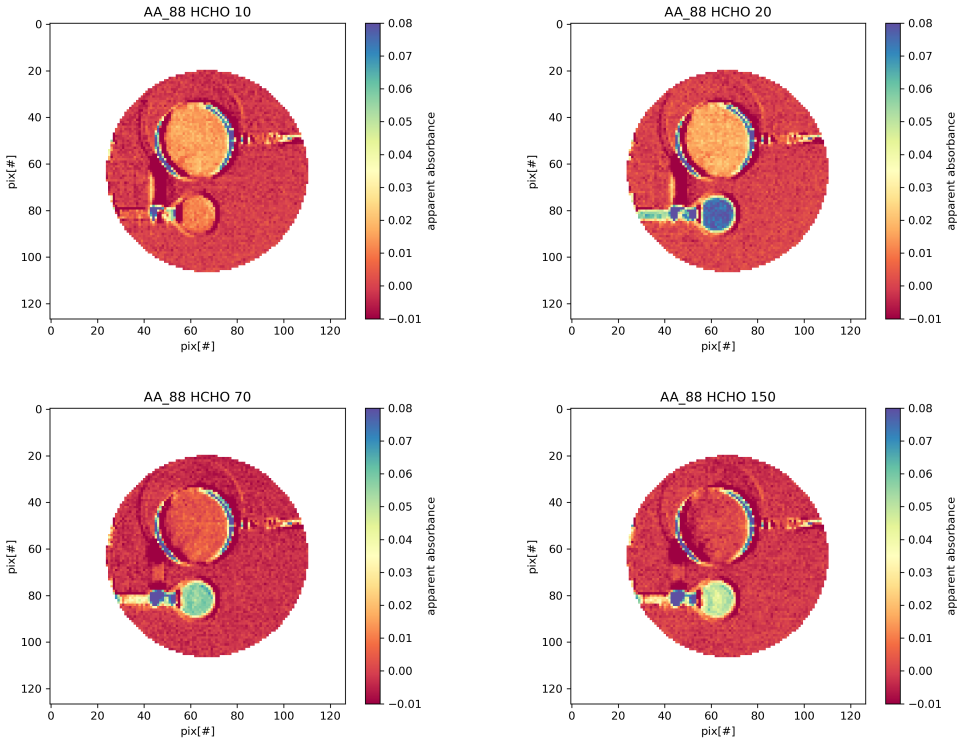

Figure 5.2.3: Image series for a HCHO gas cell measurement. Image number increases from left to right and in the two rows as well from (10,20,70,150). The AA is colour coded.

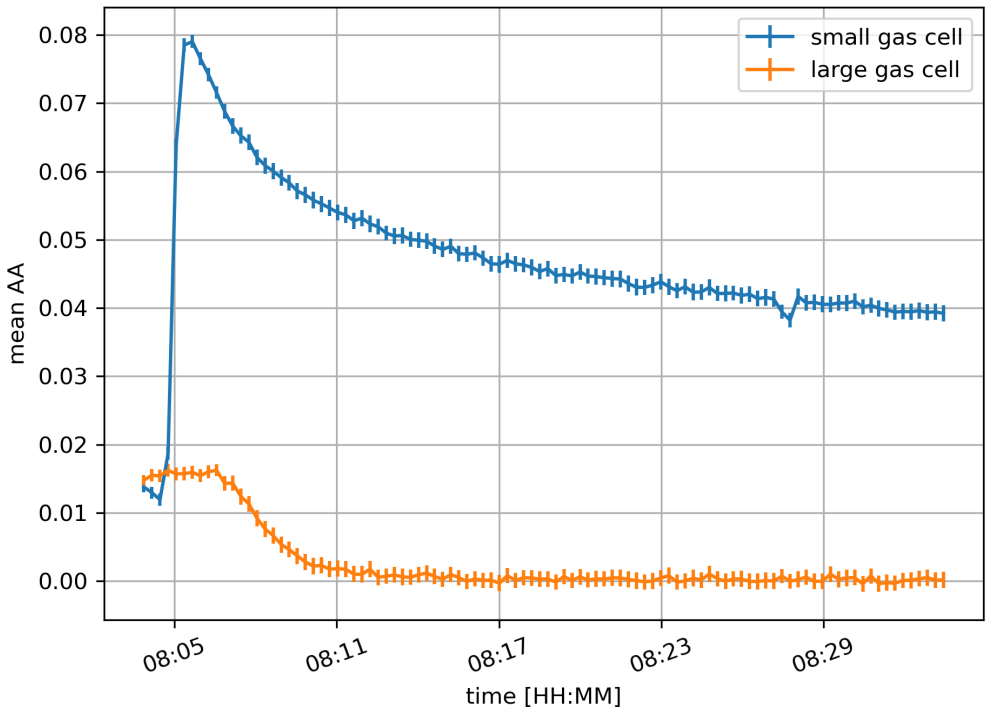

Figure 5.2.4: Mean AA for both gas cell averaged over the gas cell area plotted against the time.

0.08. The noise of the measurement lies in the range of 5% of the measured AA values. For the large gas cell the AA tends towards zero very fast and the HCHO gas has reached its equilibrium concentration after 10 min. In comparison to achieve the equilibrium concentration of gaseous HCHO in the small gas cell several hours are necessary.
The next step is to calibrate this measurement. For that purpose a parallel DOAS measurement of the gas cells is performed. The DOAS telescope is mounted next to the instrument and points into the small gas cell. To calibrate the instrument the evaluated column densities from the DOAS measurement are correlated in a scatter plot with the AA of the IFPICS measurement. Because of the low time resolution of the DOAS instrument an average over 4 IFPICS data points is necessary to compare the two measurements.

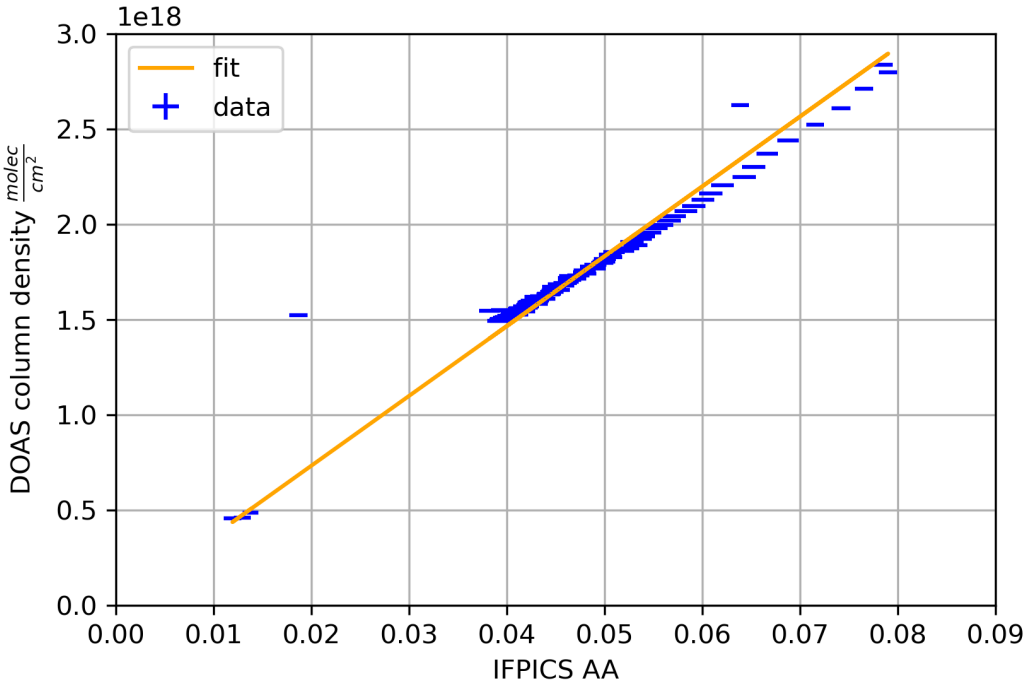

Figure 5.2.5: Scatter plot of DOAS column densities and IFPICS AA used for calibration. The data points are labelled in blue and the linear fit in orange.

The result of the correlation is shown in Figure 5.2.5. The scatter plot is fitted with a linear function, giving the following result

$$\begin{aligned} AA_{DOAS,HCHO} &= (2.72 \pm 0.01) \times 10^{-20} \frac{cm^2}{molec} \cdot S_{DOAS,HCHO} \\ S_{DOAS,HCHO} &= (3.67 \pm 0.02) \times 10^{19} \frac{molec}{cm^2} \cdot AA_{DOAS,HCHO} \end{aligned} \tag{5.2.2}$$

with a correlation coefficient of $R = 0.93$.

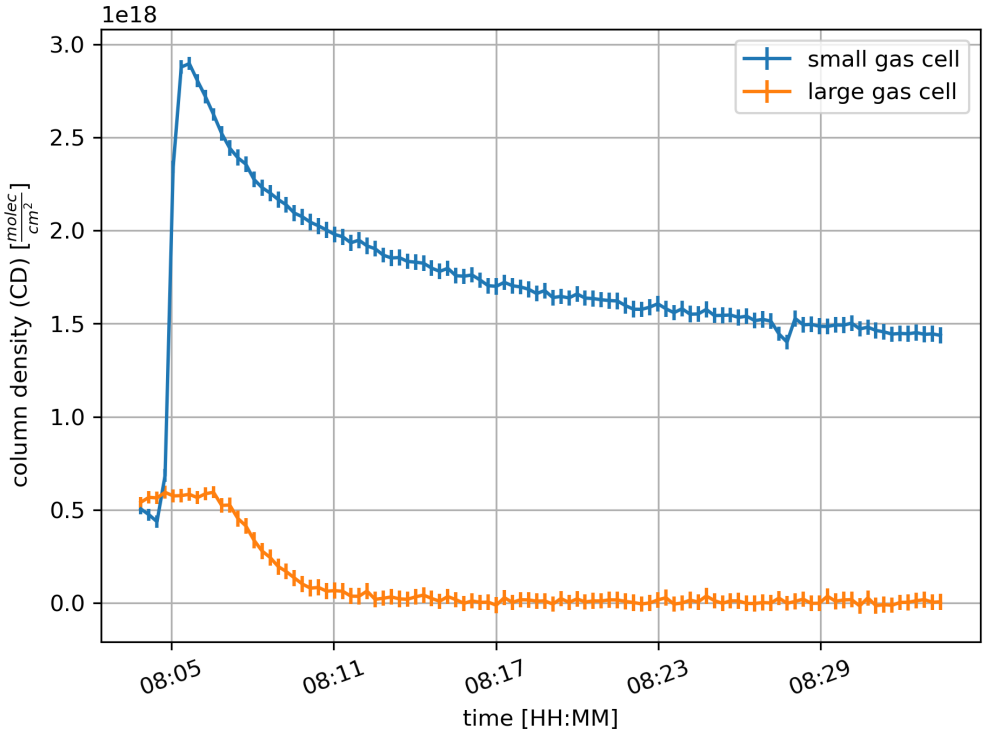

Figure 5.2.6: Column densities inside the gas cells calibrated by a DOAS measurement.

The obtained calibration function can be used to convert the apparent absorbance from 5.2.4 into HCHO column densities, which is displayed in Figure 5.2.6. After calibration the obtained maximum column density for the small cell is $2.7 \times 10^{18} molec/cm^2$ and for the large one $8 \times 10^{17} molec/cm^2$, which are very high compared to atmospheric column densities. This is beneficial for instrument testing but using a DOAS calibration in this setting has some intrinsic problems. As seen in Figure 5.2.5 the calibration is purely determined by strong signals. In this regime it is not quite clear if the assumption of a simple linear conversion still holds because of saturation effects (see section 5.1). Another important point is that the DOAS instrument looks into the small cell, which can induce gas cell effects like reflective points or effects from the edges. These artificial effects can be a possible explanation for the outliers in the calibration plot. These are likely achieved by condensation of the PFA inside the gas cell or other cell effects.

To investigate this effect further and for comparison with the expected calibration through the model a comparison of between the calibration methods is displayed in Figure 5.2.7. The solid lines show the model calibration and the dashed lines are equivalent to 5.2.6 and show the DOAS calibrated values. In both gas cell an over

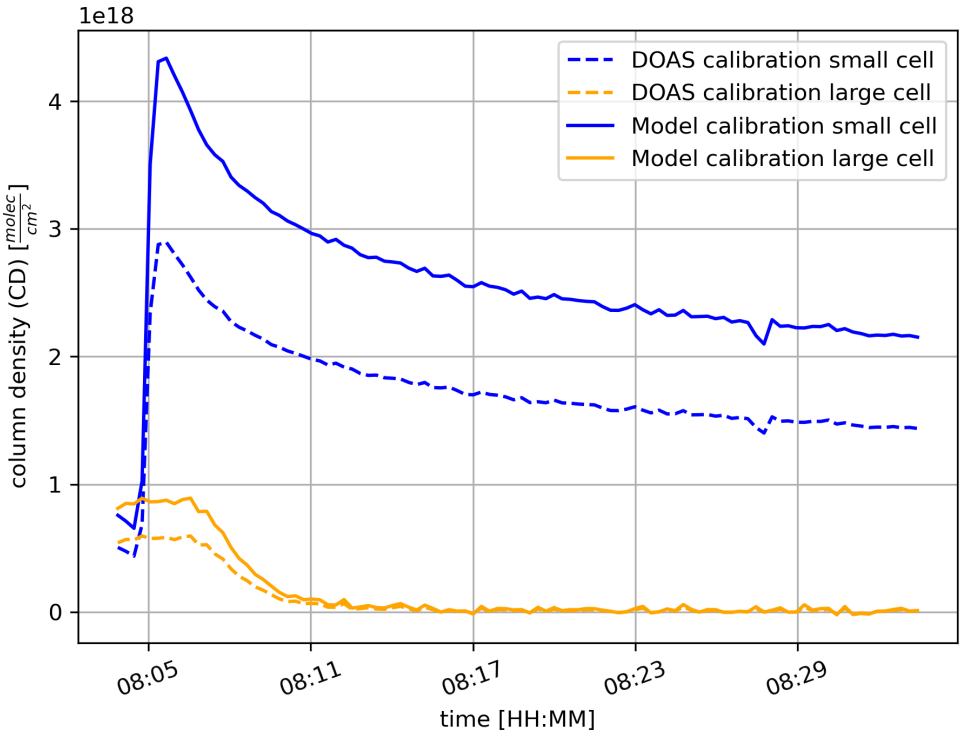

Figure 5.2.7: Comparison of the DOAS and the model calibration. The dashed lines show the DOAS calibrated values for both gas cells and the solid lines show the modelled calibration.

estimation of the model values is observed. One possible explanation are saturation effects for the high column density regime (see section 5.1). A possible solution for the saturation effects at high optical densities is to carry out the DOAS evaluation on a different wavelength range in which HCHO absorbs less and no saturation effects occur. Here, however, the wavelength range of the DOAS evaluation was chosen to be comparable to the wavelength range of the IFPICS instrument in order to compare both measurement techniques.
Summing up the measurements in this chapter, one can say that imaging of HCHO gas cell is able to give a proof of concept for measurements with the IFPICS instrument but in the future additional measurements are necessary to investigate the differences between the DOAS evaluation and the IFPICS instrument model.

6 Field measurements

After validation of the measurement principle in the laboratory using HCHO gas cells first field measurements are performed. The BrO IFPICS camera has been part of two field campaigns at Mt Etna in October 2020 (26.09.2020 - 10.10.2020) and in July 2021 (07.07.2021 - 29.07.2021). A complete list of the measuring locations can be found in the appendix A.2. The general goal of these campaigns was to validate the IFPICS principle under field conditions and test the camera system in the harsh environment of a volcano. Measurements in the field diverge drastically from the laboratory environment and several additional points have to be considered. For that reason a general discussion on parameters relevant for field measurements is given. Then a specific measurement of the second field campaign is discussed in detail. In this measurement no BrO is detected but the detection limit is determined. In addition, the SO_2 cross interference was determined under field conditions.

6.1 General remarks on field measurements with IFPICS

Before one presents the actual measurements, a short discussion on the ideal measurement geometry and locations for IFPICS measurements is given. First you have to choose a suitable position, which is first of all determined by the meteorological conditions. Ideal conditions are a cloud free sky and low wind speeds. low wind speeds reduce plume movement, which in fact reduces artificial effects due to movements of intensity gradients (plume edges) in the images (see section 4.5). Cloud free conditions are essential, because cloud cover drastically reduces sensitivity an induce several artificial effects which make a meaningful measurements much more difficult. Next, one has to consider the wind direction. Ideally one wants to have the sun in the back of the instrument to reduce effects from solar radiation (see section 4.4) and the viewing angle on the plume should be close to 90° which makes calculation of trace gas fluxes much easier. From this conditions one can conclude that westerly or easterly winds are ideal for an IFPICS instrument. The next step is to find a location where azimuthal movement of the camera yield a plume free sky region for flat field images. It is important not to change the elevation angle for flat field image acquisition. Reasons for this prerequisite are discussed in section 4.4. After choosing an appropriate location one can set up the instrument. A detailed description of the practical instrument build up is presented in the appendix A.1. Now, the imaging optics are focussed, using the camera live view and a structure far away, for example the crater edge. Afterwards the FOV composition is chosen. For

shifting of the on and off-band image as discribed in section 4.3, a strong horizontal intensity gradient is necessary, which is achieved here by moving the mountain ridge into the FOV. Another important point is to set up the FPI reflective point inside the mountain ridge (see section 4.4). After this the plume position must be settled. Ideally the plume does not cover the whole sky and still clear sky is visible to correct for the background from a point in the FOV. Finding the plume can be done by a live evaluation for SO_2 of the infield-DOAS or by employing the SO_2 FPI camera, which has been operated always next to the BrO camera on the two field campaigns. Ideally the plume shows no condensation and is completely translucent, because condensed plumes introduce errors due to movements of the plume and due to scattering processes inside the plume.
Now, the actual measurement begins by setting up the infield-DOAS measurement and with the recording of dark current images. These are performed by capping the camera optics with a dust cap. Next, flat field images are taken by turning the camera in azimuthal direction and afterwards actual plume measurements begin. Typical measurement parameters used are elevation angles of $15° - 18°$, an image resolution of 2048×2048 pixel, an exposure time of $0.3s$ and a cooling point of the detector of $0°C$. The camera operates in the UV and due to the long atmospheric light path measurement times reach from 07:00 to 15:00 UTC for the two field campaigns. This results in a detector saturation of approximately $5\% - 10\%$.

6.2 Field measurement at "Piano Vetore" (11.07.2021)

6.2.1 Conditions

The measurement presented here originates from the 11th of July and has been taken at the "Piano Vetore" (GPS position: 37.694686 N 14.977711 W) at a time between 08:24 and 09:27 UTC. The measurement location lies on the southern side of Mt Etna right next to the astrophysical observatory (OCAT) of the National Institute for Astrophysics (INAF). The distance to crater area is approximately 6 km.

In Figure 6.2.1 an image of the measurement FOV is displayed including a description of two craters visible in the FOV , i.e. the south eastern crater (SEC) and the bocca nuova crater (BNC). At this particular day both craters are outgassing but the plume from the BNC is much stronger. This can be seen from IFPICS SO_2 camera data, which was operated in parallel, by looking at the SO_2 broadband absorption through a UV bandpass filter in the live view of the camera.

The measurement geometry is shown in Figure 6.2.2. From a meteorological point of view, this day was clear of clouds and the wind was blowing from the NNW. From Figure 6.2.1 one can see, that the plume is slightly condensed. In addition, the measurement geometry is not ideal because the viewing angle on the plume is roughly 30°. A distinction of the two plumes originating from the SEC and the BNC was only possible through the SO_2 IFPICS camera.

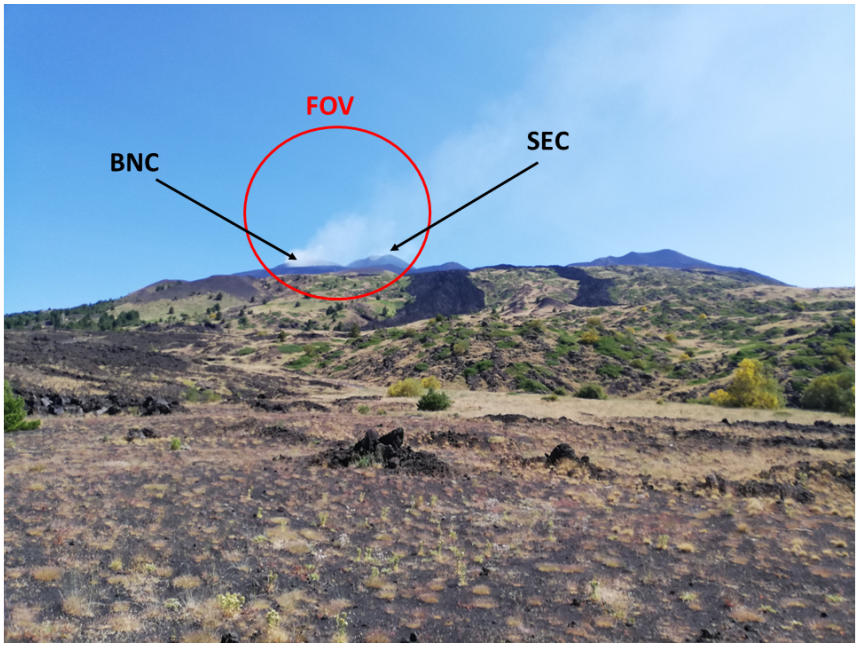

Figure 6.2.1: Image of the measurement situation. The IFPICS FOV is marked with a red circle. Visible in the FOV are two craters, Bocca Nuova crater (BNC) on the right and the South Eastern crater (SEC) on the right. Both craters are in the state of constant degassing.

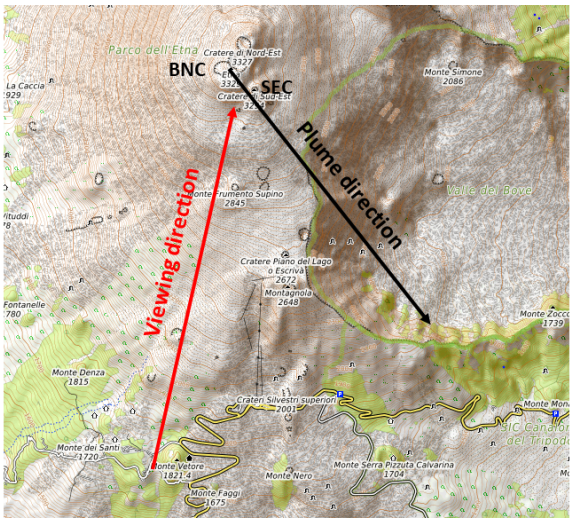

Figure 6.2.2: Map of the measurement geometry. The plume direction (coincides with the wind direction (NNW)) is marked in black and the viewing direction is marked red. (map taken from opentopomaps (2021))

The measurement consists of 100 dark current images (taken between 08:26 and 08:28 UTC) and 200 flat field images (taken between 08:33 and 08:37) taken before the plume measurement. The viewing direction for the flat field images was 342° N with an elevation angle of 18°. For the plume measurement (taken between 08:42 and 09:27) 2500 images are recorded in a viewing direction of 18° N and with the same elevation angle as the flat field images. All images are taken with an exposure time of $0.3s$ resulting in a detector saturation of approximately 5%.

6.2.2 Results

In this section a discussion on the results of the "Piano Vetore" measurement is given. First of all, a detection of BrO was not possible due to weak emissions and instrumental artefacts. But an estimation of the detection limit for BrO measurements could be obtained from this dataset. For that purpose the standard deviation of the AA signal in the background sky region is determined for different settings of spatial and temporal binning. The result is than converted via the modelled calibration factor (see section 5.1) for BrO into an estimation for the detection limit.

An image series of the detection limit calculation for a single evaluated image and different spatial binning factors is shown in Figure 6.2.3. Here no temporal binning is applied. Spatial binning increases from left to right and from the upper to the lower rows in a range from no binning up to 32×32 binning which results in a image resolution of 64×64 pixels. The actual image resolution is smaller because of the FPI clear aperture, which results in a resolution of approximately 50×50 pixel for the highest spatial binning and accordingly for lower binning factors. The area for the detection limit calculation is marked with a black box and is scaled according to the applied spatial binning starting with a dimension of 32×32 pixel for no spatial binning. The images show a strong structure in the center which originates from the reflective point of the optics (see section 3.3). In this measurement the positioning of this point is not ideal, because it is not completely covered by the crater flank. This structure is ignored in further discussion of the image series and the focus of the evaluation in this part should be on the general structure of the sky background. As shown in the model calculation an AA noise level in the range of 10^{-3} is necessary for the detection of BrO. This is not expected for a single image evaluation. Due to that an evaluation should give a homogenous noise field of the sky and no structures should be visible. Comparing this expectation to the image series, one concludes that the sky area obeys the expectation mentioned above and for every binning factor the sky area is homogeneously noisy.

To give a second insight in the detection limit calculation the same image series displayed in Figure 6.2.3 is shown in Figure 6.2.4, but with an additional temporal binning of $\approx 100s$. This averaging time is achieved by adding up 100 measurement images and taking the average of that. Compared to Figure 6.2.3 the noise level decreases drastically and even for no spatial binning structures occur. The effect of the reflective point is much more prominent and even on the left side of the images a structure due to dust on the optics occur. These structures can be easily

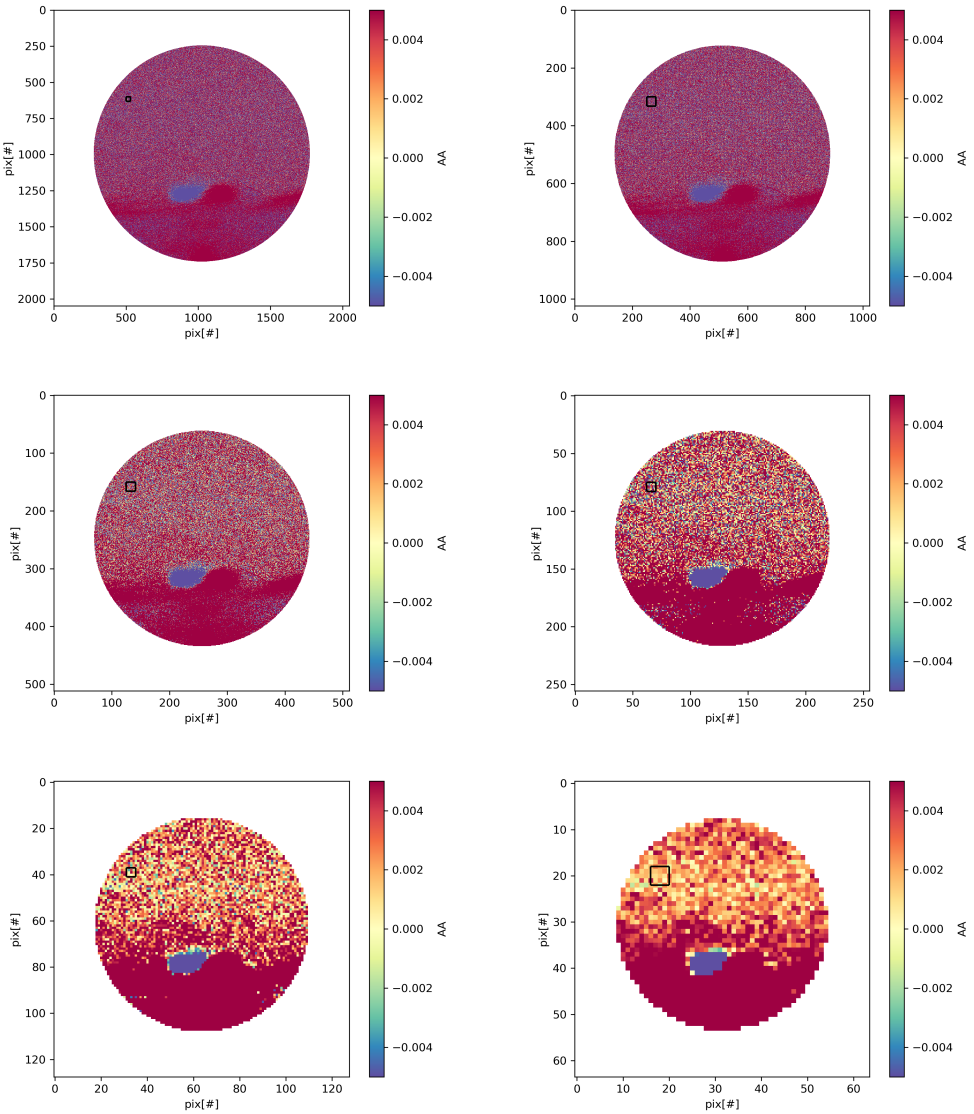

Figure 6.2.3: Image series of Piano Vetore measurement without temporal binning. The black box shows the averaging area for the AA standard deviation calculation. Images have different spatial binnings, increasing from left to right.
First row: no binning (2048 × 2048 pixel), 2 × 2 (1024 × 1024 pixel)
Second row: 4 × 4 (512 × 512 pixel), 8 × 8 (256 × 256 pixel)
Third row: , 16 × 16 (128 × 128 pixel), 32 × 32 (64 × 64 pixel)

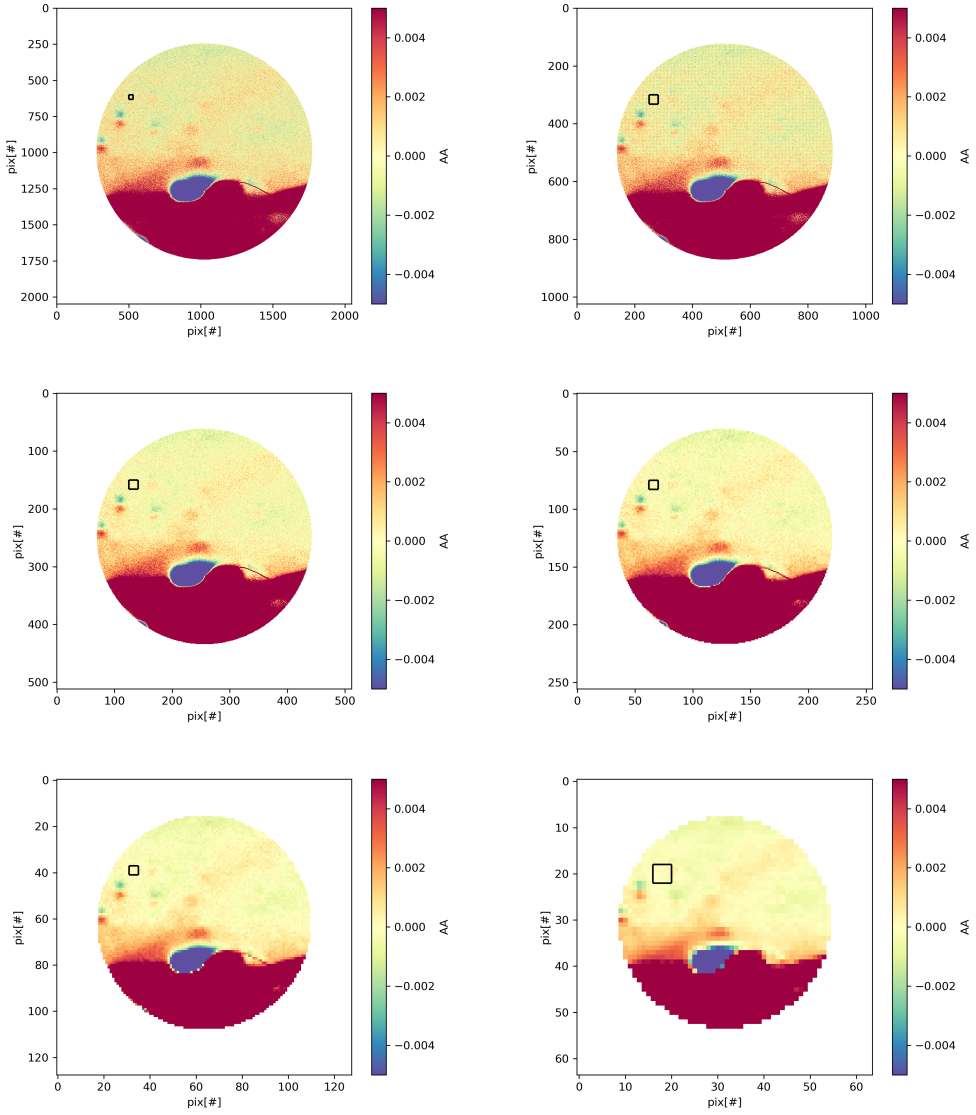

Figure 6.2.4: Image series of Piano Vetore measurement with temporal binning of $\approx 100s$. The black box shows the averaging area for the AA standard deviation calculation. Images have different spatial binnings, increasing from left to right.
First row: no binning (2048×2048 pixel), 2×2 (1024×1024 pixel)
Second row: 4×4 (512×512 pixel), 8×8 (256×256 pixel)
Third row: , 16×16 (128×128 pixel), 32×32 (64×64 pixel)

identified by a typical very high and very low signal, which is vertically aligned (see section 4.6). In addition, a possible plume signal is visible, which reaches from the left corner above the BNC upwards. This structure possibly originates from the condensed part of the plume.

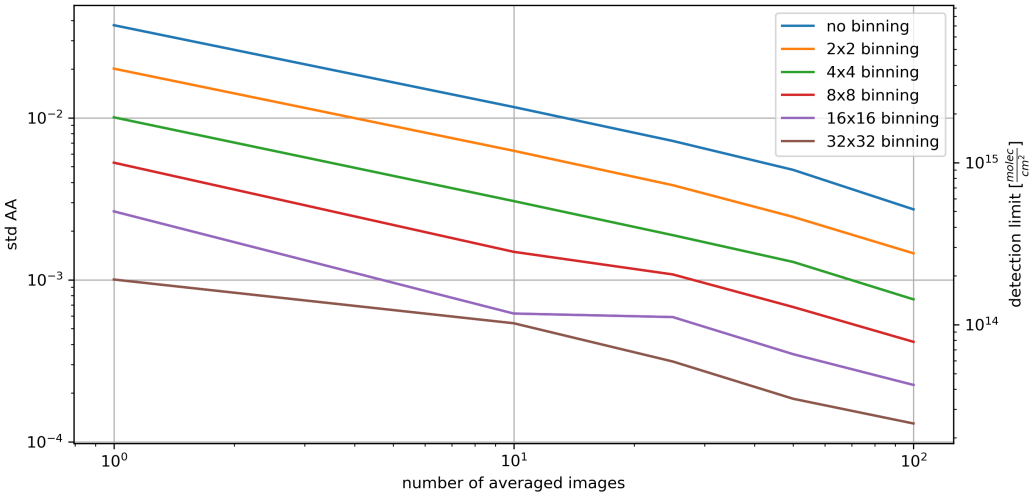

Figure 6.2.5: Detection limit plot obtained from the Piano Vetore measurement. The standard deviation of the AA in the background sky is plotted for different spatial binning factors against the number of averaged images. Additionally, the standard deviation is converted via the modelled instrument sensitivity for BrO into a detection limit in $\frac{molec}{cm^2}$.

The quantitative analysis of the detection limit calculation is displayed in Figure 6.2.5. Here the standard deviation of the black box marked in the image series of Figure 6.2.3 and Figure 6.2.4 is plotted against the number of averaged images. This is done for the following image numbers : 1, 10, 25, 50, 100. The number of averaged images corresponds to a image acquisition time with a conversion of $1s$ per image. The actual integration time of the images is smaller in the range of $0.7s$ for on-band and off-band images, but losses due to the stepper motor movement occur which explain the difference between integration time and acquisition time. Additionally, the obtained standard deviation is converted via the modelled instrument sensitivity in a detection limit for BrO in $molec/cm^2$. One can see, that for a spatial binning factor of 16×16 and a temporal average of approximately $10s$ the noise is decreased under the 10^{-3} mark. To compare these results with an expected value one can have a look at the modelled values in Kuhn et al. (2019). There a detection limit for an integration time of $10s$ and an image resolution of 51×51 pixel of $1 \times 10^{14} molec/cm^2$ is proposed. This proposal is comparable to an evaluation with a temporal binning of 10 averaged images and a spatial binning factor of 32×32, which leads to a resolution of roughly 50×50 pixel. From Figure 6.2.5 a detection limit for these

settings is obtained as $1 \times 10^{14} molec/cm^2$, which exactly matches the expectation from Kuhn et al. (2019).

6.3 SO_2 interference

Th last measurement shown in this thesis is a measurement of SO_2 gas cells. Typical volcanic BrO/SO_2 ratios lie in the range of 10^{-4}. If the camera should exploit a positive SO_2 interference measurements of BrO are not possible. To investigate this effect a measurement of SO_2 gas cells with different column densities has been done. The measurement was performed at the first field campaign at the 2nd of October 2020 between 12:12 and 12:30 UTC at the mountain ridge "Schiena dell Asino" (GPS position: 37.709601 N 15.027508 W). The viewing direction wa 15° N with an elevation angle of 50∘. The column density increases with the gas cell number between $\approx 1 - 4 \times 10^{18} molec/cm^2$. For the measurement a gas cell is held in front of the imaging optics of the instrument to cover the complete FOV. This method is used to reduce image artefacts due to moving of the gas cells, because in a filed setting no tripods are available to hold the gas cell in place.

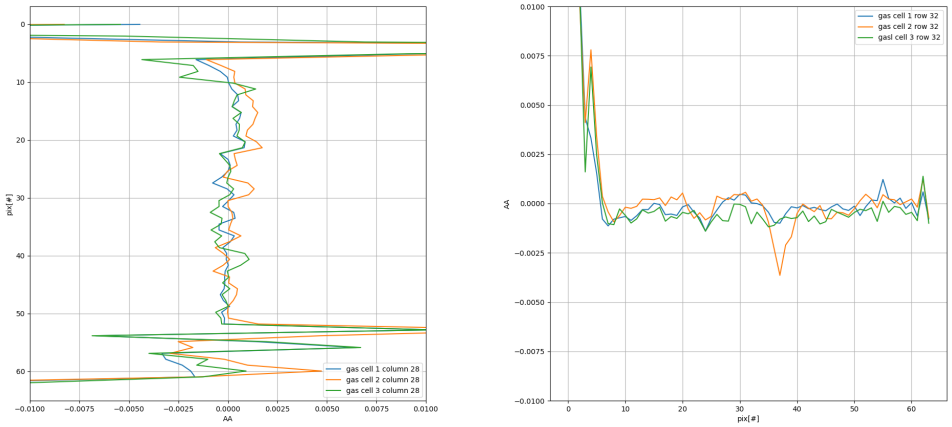

Figure 6.3.1: Plot of the AA for three SO_2 gas cells. Left panel shows column 28 and the right panel shows row 32 of the AA images.

The result of this measurement is shown in Figure 6.3.1. Here the evaluated images are binned to a resolution of 64×64 pixel to reduce noise and column 28 (left panel) and row 32 (right panel) are plotted for all three gas cells. The strong gradients at the upper and lower end of the column plot and the left side of the row plot can be ignored, because these effects originate from edges of the FOV. One can observe that the received signal for the three gas cell is almost 0. In addition, no course is visible, which would be expected if an interference to SO_2 is present. To quantify the received signal in more detail the mean value and the standard

deviation for 20 image rows is calculated, which gives the following results for the three gas cells

$$\begin{aligned} AA_{mean,1} &= (1.3 \pm 0.7) \times 10^{-4} \\ AA_{mean,2} &= (6.8 \pm 0.6) \times 10^{-4} \\ AA_{mean,3} &= (0.3 \pm 0.7) \times 10^{-4} \end{aligned} \tag{6.3.1}$$

These values support the qualitative description given above. The AA signal range is roughly one order of magnitude smaller than the expected BrO signals. The SO_2 column densities inside the gas cell are representative for normal volcanic SO_2 emissions (see Fuchs (2019)). Following this arguments, one can say that no significant SO_2 interference is expected.

7 Conclusion and Outlook

7.1 Conclusion

Imaging of weakly absorbing trace gases remains a challenging task. While imaging of volcanic SO_2 works in the 10^{-2} range of AAs, BrO and HCHO imaging in the atmosphere requires AAs in the sub 10^{-3} range. In order to reach such dimensions, a multitude of disturbing instrumental effects need to be taken care of, especially when measurements are performed under harsh volcanic field conditions.
This thesis builts on Fuchs (2019), who introduced IFPICS for volcanic SO_2. The technique is extended to the much weaker absorbing species BrO and HCHO. The prototype instrument is adapted and tested for BrO and HCHO measurements, and the optical setup and measurement software is thoroughly improved. It is shown that the instrument is capable of performing imaging measurements of larger amounts of BrO and HCHO in the atmosphere. Additionally, a detection limit for BrO is determined under field conditions
The instrumental parameters of the prototype are specified in laboratory measurements using a spectrograph setup. This includes a precise examination of the FPI , which was manufactured by SLS Optics Ltd. according to simulations in earlier works (Kuhn et al. (2019)). The wedge angle alignment, the plate separation and an angle calibration of the stepper motor was determined. In addition, the instrument development comprises the introduction of a new detector, yielding a higher quantum efficiency, which in turn results in a better SNR compared to detectors used in previous studies (e.g. Fuchs (2019)). To enhance image quality and usability in the field, the focusing optics are improved.
Furthermore, a description of the data evaluation process for IFPICS measurement images was given. Here several correction processes were shown as well as a brief discussion regarding noise sources within this instrumental setup.
The similarities of the HCHO and BrO absorption cross sections suggest that similar instrument parameters optimise the measurement of both gases, which is confirmed in model calculations. This cross interference on one hand limits BrO measurements to low HCHO backgrounds and vice versa. On the other hand, due to the difficult handling of BrO in the lab (very reactive), HCHO can be used to characterize the instrument with gas cell experiments. Further, instrument sensitivities are obtained from simulations as $k_{HCHO} = (1.8178 \pm 0.0001) \times 10^{-20} cm^2/molec$ for HCHO and $k_{BrO} = (5.288 \pm 0.002) \times 10^{-18} cm^2/molec$ for BrO. Following the results of this simulation, measurements of HCHO are investigated as a proxy for BrO. As a validation for the model simulations, angle scans of HCHO gas cells are performed giving the same on-band and off-band positions as expected from the

model simulations. This result is then used to record alternating measurements between the on-band and off-band position of the FPI of HCHO gas cells with scattered skylight as a light source. The results are compared to model simulations and DOAS measurements. Furthermore, the measurements are calibrated in two ways. Fist, with a parallel DOAS measurement, yielding an instrument sensitivity of $k_{HCHO,DOAS} = (3.10 \pm 0.08) \times 10^{-20} cm^2/molec$, and second, with the model simulations. Deviations occur for high column densities. A possible explanation for this are saturation effects. With this measurement the applicability of the IFPICS technology to HCHO imaging is shown.
After the HCHO laboratory experiments, first field measurements on two field campaigns at Mt Etna are performed to give first insights into BrO imaging in volcanic plumes and to test the instrument under field conditions. Here, the interference between SO_2 is investigated because of the high abundances of SO_2 in volcanic plumes. It is shown as expected from former simulations, that the interference is negligible. Next, a detection limit for BrO measurements is calculated from an image series recorded in the field. The result matches the prediction of Kuhn et al. (2019) revealing a detection limit for BrO of $1 \times 10^{14} molec/cm^2$ for a spatial resolution of approximately 50×50 pixels and a time resolution of 10s.

7.2 Outlook

Fast imaging of weak atmospheric absorbers remains challenging. As shown in this thesis, the IFPICS technique is a promising approach to drastically increase the spatio-temporal resolution e.g. of conventional DOAS measurements. In order to reach low detection limits, the instrument needs to be characterized very well and a high stability is required in order to sustain the instrument parameters in field conditions. A thorough routine of characterization measurements is described in this thesis.
The BrO FPI camera in the present state is an early-stage prototype. An immediate improvement should be to redesign the connection between the detector and the camera box. Currently this is achieved by a screw connection, which is error prone. If the connection is not correctly aligned, the detector may tilt. This condition is difficult to remedy, especially with sensitive optical parts, force should be applied only carefully. In addition, there may be unwanted incidence of light at the connection point, which makes the evaluation of the measurement impossible.
Another instrumental setup improvement is the addition of a sun visor to shield the optical entrance from solar radiation causing instrument stray light
After such stability and handling issues are resolved the light throughput of the instrument could be enhanced with a FPI with larger clear aperture and the corresponding optics. Thereby the noise is further reduced and higher spatial resolutions could be reached (see Kuhn et al. (2019)).
During the process of this thesis a measurement software has been developed. This software purely relies on the spyder python editor. A first improvement could be

to bring the software into a form that can be executed in the console and that only configuration files have to be adjusted. This enables the instrument to be operated by people who are not familiar with the Python programming environment. In the long term, it would be important to develop a graphical user interface (GUI), as this makes operation much easier and possibly also enables live images, which simplifies focusing and allows possible problems in the image to be corrected immediately.
This thesis has a strong focus on instrument development and testing. Nevertheless, from the two measurement campaigns at Mt Etna data exists which allow further investigation.
With refined instrument prototypes the spatial distribution of BrO in a volcanic plume could be measurable in the future. Another interesting approach could be to combine BrO imaging with other measurement methods, for example in situ measurements of other bromine species to reach a deeper understanding of volcanic halogen chemistry. Further HCHO emissions of wildfires or powerplants could be investigated. Additionally, the IFPICS technology can be extended to further trace gases as for example NO_2 or OClO.
In summary, the IFPICS technology opens up opportunities beyond present technologies to gain exciting and varied insights into atmospheric chemical processes in the future.

A Appendix

A.1 IFPICS measurement manual

In this section a detailed guide to operate the IFPICS instrument for BrO imaging in volcanic plumes is given. This description includes the infield DOAS instrument. To operate the instrument in the present state basic knowledge of DOASIS and the Python programming knowledge is required.

A.1.1 Measurement location

First, one has to choose the right measurement location. Important parameters are the relative solar azimuth angle (SAA), maybe a sheltered place in windy conditions, a stable underground and a wide azimuthal vision field. The relative SAA should be around 180°, meaning the sun is in the back of the camera FOV to reduce the influence of direct solar radiation, solar reflexes and shadows. The wide azimuthal vision field is important to take flat images by a simple azimuthal rotation without changing the elevation angle which drastically reduces gradients introduced by reference images according to section 3. An example for an ideal setup can be found in section 6. An exemplary image of the instrument setup under field conditions is shown in Figure A.1.1.

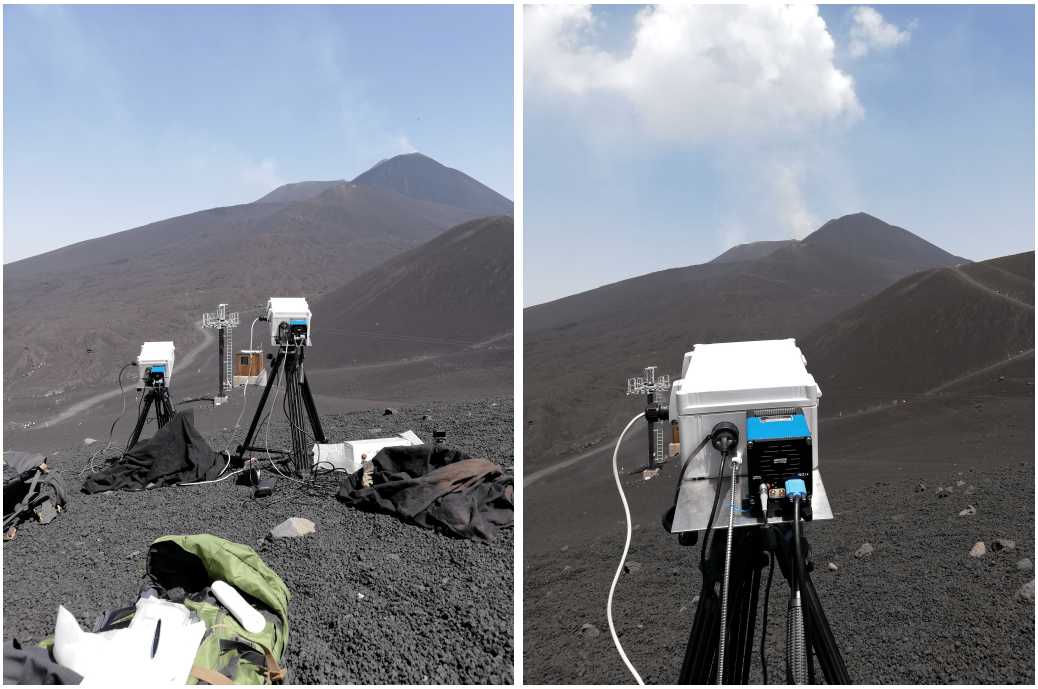

Figure A.1.1: Images of the instrument setup under field conditions.

A.1.2 Instrument assembly

In this part the instrument assembly process is described.

1. Place the tripod on a solid surface and check whether it is level. Id the instrument does not stay level, an additional correction similar to the pixel-shift in vertical direction is required to align the on-band and off-band images, which is unwanted because any additional correction is prone to errors.

2. Place the camera box on the tripod.

3. Connect the spectrograph to a $12V$ battery pack and start in order to reach the equilibrium temperature of the cooling process during the rest of the building process.

4. Install the 400μ optical fibre in the infield DOAS setup and connect it to the spectrograph.

5. Remove all dust caps inside the instrument.

6. Install FPI in correct wedge angle alignment with an $3mm$ Allen key by tighten the grub screw. The correct alignment is marked on the FPI.

7. Remove dust cap from rear instrument entrance in order to connect the detector. Install detector by connecting the rear tubus and the c-mount connection at the detector. (Attention: Avoid any jamming of the components!)

8. Connect the power supply of the detector ($24VDC$) and the $USB - C$ connection and start it to begin its cooling process.

9. Connect a second $12V$ battery pack to the camera box to power the Arduino and the stepper motor. Afterwards, connect the USB port of the camera box and the USB port of the spectrograph.

A.1.3 Measurement description

In this part the actual measurement process is described in detail. This includes a description of the IFPICS instrument and the infield DOAS instrument.

1. The measurement process starts with the initialization of the infield DOAS instrument. First, dark current (1 scan, $10s$ exposure time), offset (1000 scans, $6\mu s$ exposure time) and reference (300 scans, $(50 - 150)ms$ exposure time) spectra are taken. An optional mercury calibration can be recorded as well. Next, the mobile DOAS script is started and one uses the SO_2 live evaluation for example to find the plume.

2. Focussing of the camera is achieved through the live view of the pco software package *pco.camware64*. One has to loosen the detector on the rail system and adjust its distance to th camera box by moving the tunable tube inside the camera box until a sharp image is achieved. This can be checked by looking at a point far away in the FOV for example a crater flank.

3. Adjust the elevation angle of the instrument to check that the reflective point of the optical setup is set for example in the crater flank to have an interference free image. In addition, change the azimuthal direction of the instrument to check if it is possible to take flat field images without changing the elevation angle of the instrument. If both points are achieved, fix the detector on the rail system that it cannot move by mistake.

4. Check the saturation of the detector to choose the smallest possible integration time. In general an integration time of $0.3s$ yields approximately 2000 counts.

5. Open the measurement script and determine GPS position, azimuth and elevation angle of the measurement and fill this into the measurement script. Determine the integration time, initialization number and and image type and set it up in the measurement script as well. Usually three image types are used (dc (dark current images), flat (flat field images), tg (trace gas images)).

6. In general the measurement is started with dark images. For that choose dc in the measurement script and put a dust cap on the instrument. Then start the script for example with 50 images and 2 initializations.

7. Remove dust cap change image type to flat and move the instrument to a plume free sky region. Adjust the viewing direction and take flat field images (e.g. 200 images with 4 initializations)

8. Move azimuth direction towards the plume region again and try to find a position where the infiled DOAS looks into the plume and ideally shows a strong variation which makes correlation between IFPICS and DOAS data easier. One aims to have the plume, a plume free sky region and a clear intensity gradient (for image alignment) in the FOV. Then change image type to tg in the script and adjust the initialization number according to the preferred measurement time (e.g. 500 initializations for a measurement of approximately $90min$ at a exposure time of $0.3s$).

9. The previous three points can be repeated several times. But data storage has to be monitored because 1 image requires a storage capacity of $8MB$.

10. In case of an emergency stop the script can be finished by simply inserting $Ctrl + c$ in the python console

A.1.4 Common problems and solutions

In this section common problems according the measurement software and the instrument assembly are discussed.

1. Problems with the Arduino software and the serial connection are usually solved by a reconnection and in rare cases a reconnection and a restart of the python kernel.

2. in case of a jammed detector connection one can remove the complete tube from the camera box. It is important to tilt the instrument forward because the rear tube holds lens pair 2 at its place.

3. To check if th connection of detector and camera fits appropriate look at the live view for a dark current image. Here possible light intrusions are visible. This should be done before every measurement.

A.2 Measurement locations for both field campaigns

In this section an overview over the measurement location of the field campaigns at Mt Etna is given.

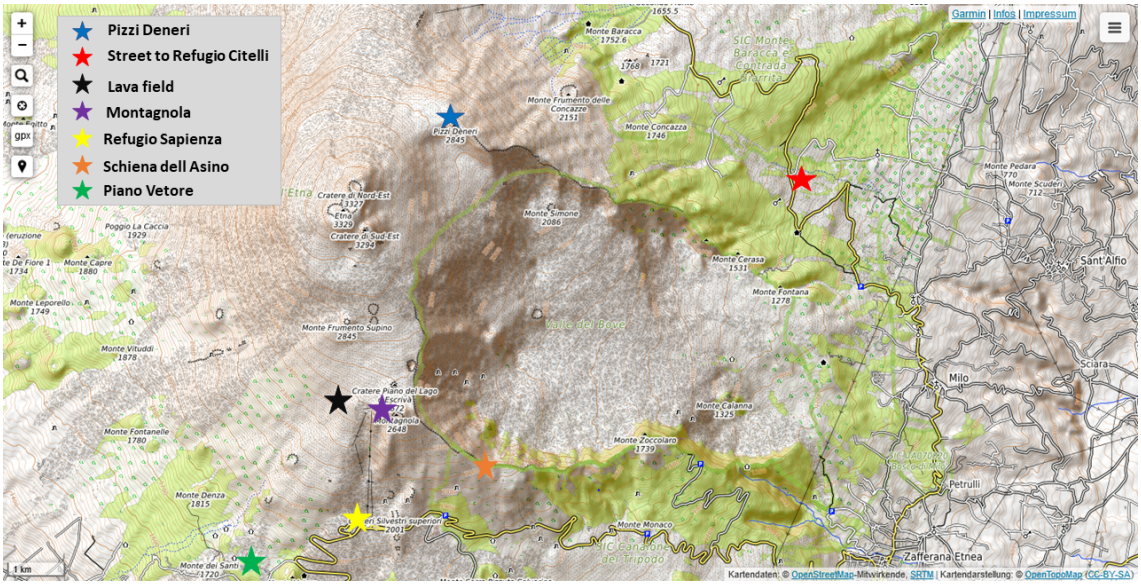

Figure A.2.1: Measurement locations for both field campaigns. The locations are marked with coloured stars. (map from opentopomaps (2021))

The measurement locations are marked with coloured stars on the map of Mt Etna shown in Figure A.2.1. The positions are chosen according to the procedure described in A.1.1.

In Table A.1 and Table A.2 a detailed overview over the measurement days is given, including the camera elevation and the viewing direction. The measurement time indicates the complete measurement duration on the respective day, including the dark and flat field measurements.

Date [dd.mm.yyyy]	GPS position	Time [UTC]	Viewing direction [°]	Elevation angle [°]
30.09.2020	37.58649 15.168478	06:57 - 07:12	288° W	17°
30.09.2020	37.721146 15.001019	12:12 - 12.22	45° N	15°
01.10.2020	37.718938 15.004086	08:15 - 10.28	8° N	15°
02.10.2020	37.709601 15.027508	08:26 - 12:02	25° N	13°
08.10.2020	37.720027 14.999108	08:13 - 09:52	13° N	20°
09.10.2020	37.692708 14.973006	07:27 - 09:09	30° N	20°

Table A.1: Measurement locations for the first field campaign at Mt Etna between 25th of September 2020 and 11th of October 2020.

Date [dd.mm.yyyy]	GPS position	Time [UTC]	Viewing direction [°]	Elevation angle [°]
11.07.2021	37.694686 14.977711	08:13 -10:35	18° N	18°
13.07.2021	37.717822 14.998946	08:15 - 12:39	347° N	17°
15.07.2021	37.527603 15.020858	07:55 - 10:06	335° N	18°
21.07.2021	37.765715 15.016574	08:50 - 11:31	230° SW	17°
24.07.2021	37.764945 15.017277	07:15 - 12:28	230° SW	18°
25.07.2021	37.71901 15.00364	07:56 -11:34	350° N	14°
26.07.2021	37.719219 15.003688	08:24 - 11:21	323° NW	14°

Table A.2: Measurement locations for the first field campaign at Mt Etna between 07th of July 2020 and 29th of July 2021.

B Lists

B.1 List of Figures

B.2 List of Tables

C Bibliography

P. AG. pco edge 4.2 bi datenblatt. Technical report, 2021.

E. M. V. Association. Emva standard 1288 standard for characterization of image sensors and cameras. Technical report, European Machine Vision Association, 2021.

L. A. Barrie, J. W. Bottenheim, R. C. Schnell, P. J. Crutzen, and R. A. Rasmussen. Ozone destruction and photochemical reactions at polar sunrise in the lower arctic atmosphere. *Nature*, 1988. doi: doi:10.1038/334138a0.

G. Bluth, J. Shannon, I. Watson, F. Prata, and V. Realmuto. Development of an ultra-violet digital camera for volcanic sulfur dioxide imaging. *Journal of Volcanology and Geothermal Research*, 2007.

N. Bobrowski and G. Giuffrida. Bromine monoxide / sulphur dioxide ratios in relation to volcanological observations at mt. etna 2006–2009. *Solid Earth*, 2012. doi: doi:10.5194/se-3-433-2012.

K. Chance and R. L. Kurucz. An improved high-resolution solar reference spectrum forearth's atmosphere measurements in the ultraviolet, visible, and near infrared. *Journal of Quantitative Spectroscopy and Radiative Transfer*, 2010. doi: 10.1016/j.jqsrt.2010.01.036.

K. Chance and J. Orphal. Revised ultraviolet absorption cross sections of hcho for the hitran database. *Journal of Quantitative Spectroscopy and Radiative Transfer*, 2011. doi: https://doi.org/10.1016/j.jqsrt.2011.02.002.

W. Demtroeder. *Experimentalphysik 2*. Springer, Berlin, Heidelberg, 2013. doi: https://doi.org/10.1007/978-3-642-29944-5.

A. S. Dinger, K. Stebel, M. Cassiani, H. Ardeshiri, C. Bernardo, A. Kylling, S. Park, I. Pisso, N. Schmidbauer, J. Wasseng, and A. Stohl. Observation of turbulent dispersion of artificially released so2 puffs with uv cameras. *Atmospheric MeasurementTechniques*, 2018. doi: https://doi.org/10.5194/amt-11-6169-2018.

ehd imaging GmbH. Uv-camera scm2020-uv. Technical report, 2021. URL `https://ehd.de/products/specialapplications/SCM2020-UV.pdf`.

G. Farnebaeck. Fast and accurate motion estimation using orientation tensors and parametric motion models. In *Proceedings of 15th International Conferenceon Pattern Recognition*, 2000.

O. C. Fleischmann, M. Hartmann, J. P. Burrows, and J. Orphal. New ultravioletabsorption cross-sections of bro at atmospheric temperatures measured by time windowing fourier transform spectroscopy. *Journal of Photochemistry and Photobiology*, 2004. doi: https://doi.org/10.1016/j.jphotochem.2004.03.026.

C. Fuchs. Imaging of volcanic trace gases by fabry-perot interferometer correlation spectroscopy. Master's thesis, University of Heidelberg, 2019.

C. Fuchs, J. Kuhn, N. Bobrowski, and U. Platt. Quantitative imaging of volcanic so2 plumes using fabry–pérot interferometer correlation spectroscopy. *Atmospheric Measurment Techniques*, 2021. doi: https://doi.org/10.5194/amt-14-295-2021.

J. F. Grainger and J. Ring. Anomalous fraunhofer line profiles. *Nature*, 1962. doi: https://doi.org/10.1038/193762a0,.

A. Gutmann, N. Bobrowski, T. Roberts, J. Ruediger, and T. Hoffman. Advances in bromine speciation in volcanic plumes. *frontiers in Earth Science*, 2018. doi: https://doi.org/10.3389/feart.2018.00213.

E. P. Kantzas, A. J. S. McGonigle, G. Tamburello, A. Aiuppa, and R. G. Bryant. Protocols for uv camera volcanic so2 measurements. *Journal of Volcanology and Geothermal Research*, 2010. doi: https://doi.org/10.1016/j.jvolgeores.2010.05.003.

C. Kern, F. Kick, P. Luebcke, L. Vogel, M. Woehrbach, and U. Platt. Theoretical description of functionality, applications, andlimitations of so2 cameras for the remote sensing of volcanic plumes. *Atmospheric Measurement Techniques*, 2010. doi: doi:10.5194/amt-3-733-2010.

C. Kern, P. Luebke, N. Bobrowski, R. Campion, T. Mori, J. Smekens, K. Schrebel, G. Tamburello, M. Burton, U. Platt, and F. Prata. Intercomparison of so2 camera systems for imaging volcanic gas plumes. *Journal of Volcanology and Geothermal Research*, 2014. doi: https://doi.org/10.1016/j.jvolgeores.2014.08.026.

J. Kuhn, N. Bobrowski, P. Luebke, L. Vogel, and U. Platt. A fabry–perot interferometer-based camera for two-dimensional mapping of so2 distributions. *Atmospheric Measurement Techniques*, 2014. doi: https://doi.org/10.5194/amt-7-3705-2014.

J. Kuhn, U. Platt, N. Bobrowski, and T. Wagner. Towards imaging of atmospheric trace gases using fabry–pérot interferometer correlation spectroscopy in the uv and visible spectral range. *Atmospheric Measurement Techniques*, 2019. doi: https://doi.org/10.5194/amt-12-735-2019.

F. Lohberger, G. Hönninger, and U. Platt. Ground-based imaging differential optical absorption spectroscopy of atmospheric gases. *Applied Optics*, 2004. doi: doi: 10.1364/ao.43.004711.

I. Louban, N. Bobrowski, D. Rouwet, S. Inguaggiato, and U. Platt. Imaging doas for volcanological applications. *Bulletin of Volcanology*, 2009. doi: https://doi.org/10.1007/s00445-008-0262-6.

P. Luebcke, N. Bobrowski, S. Illing, C. Kern, J. M. A. Nieves, L. Vogel, J. Zielcke, H. D. Granados, and U. Platt. On the absolute calibration of so2 cameras. *Atmospheric Measurement Techniques*, 2013. doi: https://doi.org/10.5194/amt-6-677-2013.

H. McElhoe and W. Conner. Remote measurement of sulfur dioxide emissions using an ultraviolet light sensitive video system. *Journal of the Air Pollution Control Association*, 1986. doi: https://doi.org/10.1080/00022470.1986.10466043.

T. Mori and M. Burton. The so2 camera: A simple, fast and cheap method for ground-based imaging of so2 in volcanic plumes. *Geophysical Research Letters*, 2006. doi: 10.1029/2006gl027916.

opentopomaps, Aug. 2021. URL https://opentopomap.org/#map=5/49.000/10.000.

C. Oppenheimer, T. Fischer, and B. Scaillet. *Treatise on Geochemistry*, chapter Volcanic Degassing: Process and Impact, pages 111–180. Elsevier, 2014. doi: 10.1016/B978-0-08-095975-7.00304-1.

U. Platt, P. Luebke, J. Kuhn, N. Bobrowski, F. Prata, M. Burton, and C. Kern. Quantitative imaging of volcanic plumes — results, needs, and future trends. *Journal of Volcanology and Geothermal Research*, 2015. doi: https://doi.org/10.1016/j.jvolgeores.2014.10.006.

M. Polyanskiy. Refractive index database. Technical report, 2021. URL https://refractiveindex.info.

W. Roedel and T. Wagner. *Physik unserer Umwelt: Die Atmosphäre*. Springer Spektrum, Berlin, Heidelberg, 2017. doi: https://doi.org/10.1007/978-3-662-54258-3.

Danksagungen

An dieser Stelle möchte ich mich bei all denjenigen bedanken, die mich während der Anfertigung dieser Masterarbeit unterstützt und motiviert haben.

Zuerst möchte ich mich bei Prof. Dr. Ulrich Platt bedanken für die Betreuung und Begutachtung der Masterarbeit und insbesondere für die Möglichkeit an Messkampagnen und Konferenzen teilzunehmen.

Zusätzlich möchte ich mich bei Prof. Dr. Thomas Wagner bedanken für die unkomplizierte Übernahme der Zweitkorrektur meiner Masterarbeit.

Ein besonderer Dank geht an Jonas und Chris für die ausgezeichnete Betreuung und die enorme Unterstützung bei der Umsetzung der gesamten Arbeit.

Des Weiteren möchte ich mich bei Nicole bedanken, die mich mit Ihrer Begeisterung für Vulkane angesteckt hat.

Natürlich möchte ich mich auch bei Jonas, Chris, Nicole, Mia und Simon für die Unterstützung beim Korrekturlesen bedanken.

Herzlich bedanken möchte ich mich auch bei meiner Freundin Mia, die mich immer wieder ermutigt und mit vielen nützlichen Tipps einen wesentlichen Teil zur Masterarbeit beigetragen hat.

Zuletzt, möchte ich mich bei meiner Familie bedanken, insbesondere meinen Eltern, die mir mein Studium ermöglicht und mich in all meinen Entscheidungen unterstützt haben.

Erklärung:

Ich versichere, dass ich diese Arbeit selbstständig verfasst habe und keine anderen als die angegebenen Quellen und Hilfsmittel benutzt habe.

Heidelberg, den 31. August 2021 .....  .....